



VRIJE
UNIVERSITEIT
BRUSSEL

Vrije Universiteit Brussel
Faculteit Wetenschappen en
Bio-ingenieurswetenschappen
Departement Natuurkunde

1

2

3

4

5

6

7

Search for Dark Matter in the Monojet
and Trackless Jets Final States with
the CMS Detector at the LHC

Isabelle De Bruyn

8

9

Promotor
Prof. Dr. Steven Lowette

10

11

Proefschrift ingediend met het oog op het behalen van de
academische graad van Doctor in de Wetenschappen

12

September 2017

Acknowledgements

Table of Contents

1

2	Acknowledgements	i
3	1 Introduction	1
4	2 Dark Matter Scenarios Beyond the Standard Model	3
5	2.1 The Standard Model of Particle Physics	3
6	2.1.1 Elementary particles and their interactions	3
7	2.1.2 The theoretical framework of the Standard Model	4
8	2.1.3 Unanswered questions of the Standard Model	5
9	2.2 Dark matter	6
10	2.2.1 Observational evidence	6
11	2.2.2 Dark matter models	9
12	2.2.3 Detection of dark matter	10
13	2.2.3.1 Direct detection experiments	10
14	2.2.3.2 Indirect detection experiments	11
15	2.2.3.3 Collider experiments	11
16	2.3 Strongly Interacting Massive Particles	11
17	2.3.1 The SIMP simplified model	11
18	2.3.2 Experimental constraints	12
19	3 The LHC and the CMS Detector	15
20	3.1 The Large Hadron Collider at CERN	15
21	3.1.1 The LHC injector chain	15
22	3.1.2 The Large Hadron Collider	16
23	3.1.3 The experiments at the LHC	17
24	3.2 The CMS detector	17
25	3.2.1 The tracker	18
26	3.2.1.1 The pixel tracker	19
27	3.2.1.2 The strip tracker	20
28	3.2.2 The electromagnetic calorimeter	20
29	3.2.3 The hadronic calorimeter	21
30	3.2.4 The muon system	23
31	3.2.5 Trigger and data acquisition	24
32	3.2.6 CMS performance in Run 2	25
33	3.2.6.1 Pre-amplifier saturation in the APV25 chip	26
34	4 Event Simulation and Reconstruction	29
35	4.1 Event generation	29
36	4.2 Detector simulation	30
37	4.3 Event reconstruction	31
38	4.3.1 Track reconstruction	31
39	4.3.2 Electron and isolated photon reconstruction	32
40	4.3.3 Muon reconstruction	33
41	4.3.4 Particle flow	33
42	4.3.5 Jet reconstruction	34
43	4.3.6 Missing transverse energy reconstruction	35
44	4.4 Simulation of the SIMP signal	36

1	5 The Monojet Analysis	39
2	5.1 Introduction	39
3	5.2 Event selection	39
4	5.3 Background estimation	39
5	5.4 Results	39
6	5.5 Improvement going from the 2015 to 2016 analysis	39
7	5.6 Interpretation	39
8	6 Search for SIMPs using Trackless Jets	41
9	6.1 Introduction	41
10	6.2 Event selection	41
11	6.3 Background estimation	41
12	6.4 Results	41
13	6.5 SIMP model interpretation	41
14	7 Conclusion & Outlook	43

1

Introduction

1

2

2

1

2

3

Dark Matter Scenarios Beyond the Standard Model

4 In modern particle physics, the fundamental structure of matter at subatomic scales is described by the
5 **Standard Model**, which has already explained many experimental results and is today considered among
6 the most thoroughly tested scientific theories. The Higgs boson, the last missing piece which was pre-
7 dicted more than 50 years ago, was recently discovered at the Large Hadron Collider (**LHC**) in 2012,
8 thus completing this elegant theory. Although it has survived many precision tests so far, the Standard
9 Model only describes 5% of the matter and energy in the known universe and is unable to explain many
10 unresolved questions and observations, such as the baryon asymmetry, dark matter and dark energy, the
11 neutrino masses, the incorporation of gravity, and the hierarchy problem.

12 In this chapter, a brief description of the Standard Model is first given in Section 2.1, including its
13 shortcomings. In Section 2.2, one of the missing pieces in the Standard Model, dark matter, is discussed.
14 The observational evidence for dark matter, as well as possible models and detection mechanisms are
15 detailed. Finally, in Section 2.3 one of the dark matter models considered in this thesis is described in
16 detail.

2.1 The Standard Model of Particle Physics

18 The Standard Model of elementary particle physics has been developed during the second half of the
19 20th century, and **reached its current formulation in the 1970's with the experimental confirmation of the**
existence of quarks. It is a quantum field theory which describes the fundamental particles and their in-
21 teractions, incorporating three of the four fundamental forces. While this consistent framework describes
22 the electromagnetic force and the weak and strong nuclear interactions, the fourth interaction, gravity, has
23 not yet been included successfully.

2.1.1 Elementary particles and their interactions

25 All ordinary matter we see around us is build up from atoms, which consist of negatively charged electrons
26 circulating around the positively charged atomic nucleus, formed by protons and neutrons, which in turn
27 consist of up and down quarks. The electrons and up and down quarks are fundamental particles called
28 fermions. Although all ordinary matter can be build from this so-called first generation of fermions,
29 there are twelve fermions with different **flavours** in total, six quarks and six leptons, grouped in three
30 generations with increasing mass, as shown in Figure 2.1. **The electrically neutral neutrinos interact very**

¹ weakly with matter, which complicates their observation, but they can be detected in very large dedicated
² experiments.

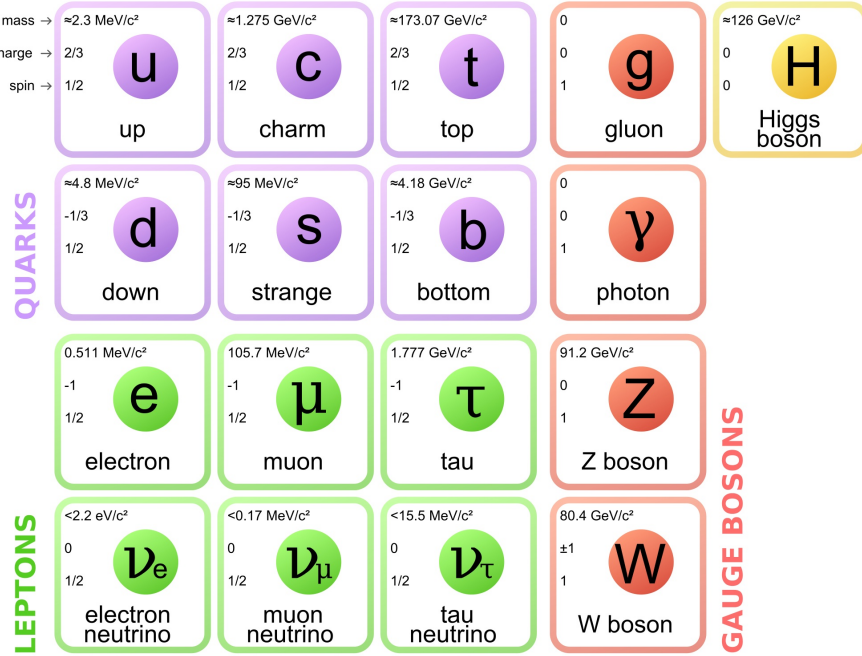


Figure 2.1: The particle content of the Standard Model, showing the fermions divided into 3 generations (columns) on the left and the bosons on the right. The electrical charges are expressed as multiples of the absolute value of the electron charge. Figure taken from [1].

³ A common characteristic of the fermions is their half-integer spin, in contrast to the integer spin of
⁴ the force mediators, called bosons. Within the Standard Model, the mediation of the different fundamental
⁵ interactions is represented by the exchange of these spin-1 gauge bosons, which are summarized in
⁶ Figure 2.1. The massless photon mediates the most familiar force, the electromagnetic interaction, which
⁷ is responsible for light, electromagnetic fields, and chemical reactions. The weak nuclear interaction is
⁸ used to describe the radioactive decay, and is propagated by the neutral Z boson and two charged
⁹ massive W bosons. Lastly, the strong nuclear interaction is carried by massless gluons, keeping the protons
¹⁰ and neutrons in the atomic nuclei and holding the quark constituents together. A resulting property
¹¹ of the quarks is that hadronize, i.e. they cannot exist isolated, but form bound states via the strong interaction,
¹² called hadrons. Hadrons made up from three quarks are referred to as baryons, while bound states
¹³ consisting of a quark and an anti-quark are called mesons.

¹⁴ Finally, it is also important to note that for every fermion there exists an anti-fermion, which differs
¹⁵ only in electric charge and handedness of spin, denoted with a bar above the particle symbol. When
¹⁶ matter and anti-matter come into contact they annihilate, generating energy which is transformed into
¹⁷ other particles.

¹⁸ 2.1.2 The theoretical framework of the Standard Model

¹⁹ The Standard Model goes further than merely giving an exhaustive list of elementary particles, it has a
²⁰ supporting theoretical framework formulated as a relativistic quantum field theory. In a quantum field
²¹ theory, every particle is represented by discrete excitations of a field $\psi(x)$, where x is the space-time
²² coordinate. The interactions and kinematics of this particle are fully determined by the action S , which
²³ is defined as the integral of the Lagrangian $\mathcal{L}(\psi(x), \partial^\mu \psi(x))$ over the space-time coordinates:

$$S = \int \mathcal{L}(\psi(x), \partial^\mu \psi(x)) d^4x. \quad (2.1)$$

1 The Lagrangian is a function of the field $\psi(x)$ and its first derivative $\partial^\mu\psi(x)$, where μ represents the
 2 index of the space-time coordinate. The physical behaviour of the particles is obtained by following the
 3 principle of least action $\delta S = 0$, minimizing the action.

4 In this framework based on the gauge invariance of the Lagrangian under the fundamental forces,
 5 the interactions between the fermions and bosons follow automatically. This can be illustrated with the
 6 following example for invariance under a general local gauge transformation.

7 As mentioned before, a fermion has a half integer spin and can thus be represented as a complex
 8 relativistic spin-1/2 field, called a Dirac spinor:

$$\mathcal{L}_{Dirac} = i\bar{\psi}\gamma^\mu\partial_\mu\psi - m\bar{\psi}\psi, \quad (2.2)$$

9 where γ^μ are the Dirac matrices, and the adjoint field $\bar{\psi} = \psi^\dagger\gamma^0$ is the field associated to the anti-fermion.
 10 The imposed local gauge invariance then requires the fermion fields, and the overall Lagrangian, to be
 11 invariant under so-called local phase transitions

$$\psi \rightarrow \psi' = U(x)\psi = e^{i\vec{\alpha}(x) \cdot \frac{\vec{\tau}}{2}}\psi \quad (2.3)$$

12 where $\vec{\alpha}(x)$ are the space-time dependent rotation parameters in the symmetry group represented by the
 13 Lie group generators $\vec{\tau}$. Since the derivative ∂_μ in (2.2) spoils the invariance of the Lagrangian under a
 14 local phase transformation, it is replaced with a covariant derivative

$$D_\mu = \partial_\mu - ig\frac{\vec{\tau}}{2}\vec{A}_\mu, \quad (2.4)$$

15 restoring the invariance. This however introduces new vector gauge fields A_μ , which interact with the
 16 fermion fields with a coupling strength g . As a result, the Dirac Lagrangian contains an additional term,
 17 which describes the interaction between the fermion fields mediated by the gauge fields A_μ , and (2.2)
 18 becomes

$$\mathcal{L}_{Dirac} = i\bar{\psi}\gamma^\mu\partial_\mu\psi - m\bar{\psi}\psi + g\bar{\psi}\gamma^\mu\psi\vec{A}_\mu \cdot \frac{\vec{\tau}}{2} \quad (2.5)$$

19 **TODO: interactions, higgs, CP-violation**

20 **2.1.3 Unanswered questions of the Standard Model**

21 Although the Standard Model is an extremely successful theory, there are still many questions that remain
 22 unanswered, indicating that the Standard Model cannot be a complete theory of nature. A brief description
 23 of some of the main unsolved problems follows here.

24 **Grand Unified Theory**

25 As the weak and electromagnetic interactions were successfully unified into the electroweak one,
 26 the idea of representing the three forces of the Standard Model by a single one is envisaged and
 27 studied. While this Grand Unified Theory (GUT) could be a first step towards the incorporation of
 28 gravity in the Standard Model, it cannot be achieved with the current Standard Model and requires
 29 new physics at a very high energy scale.

30 **Baryon asymmetry**

31 This problem refers to the imbalance of matter and anti-matter in the universe. While the Big
 32 Bang should have produced an equal amount of baryonic and anti-baryonic matter, this is not
 33 measured in our observable universe. It is assumed that most of the primordial matter and anti-
 34 matter annihilated, but an imbalance allowed a fraction of the matter to survive. Within the Standard
 35 Model, some asymmetry in the production of matter and anti-matter could be explained by the CP-
 36 violation of the weak interaction. However, the amount of CP-violation needed to explain the
 37 baryon asymmetry is ten times higher than is observed from Standard Model measurements.

38 **Hierarchy problem**

39 The most important hierarchy problem concerns the question why the weak force is so much

1 stronger than gravity. The measured vector boson masses suggest that the electroweak symmetry
 2 breaking should occur at an energy scale of $\mu^2 \sim (100 \text{ GeV})^2$, while the energy regime
 3 where gravity becomes comparable to the other forces, called the Planck scale, is of the order
 4 of $\Lambda_{\text{Planck}} \sim 10^{19} \text{ GeV}$. This would require a significant fine-tuning of at least 28 orders of mag-
 5 nitude, which is not desirable for any theory.

6 Dark matter and energy

7 This mystery arises from cosmological observations, which indicate that the known matter de-
 8 scribed by the Standard Model makes up only 5% of the matter and energy in the universe. The
 9 remaining matter, called dark matter, contributes another 27%, and will be discussed in more detail
 10 in Section 2.2. In the Standard Model, neutrinos could contribute to the dark matter, but their relic
 11 density would not be enough to account for all the dark matter. The last 68% has been labelled dark
 12 energy and is believed to be responsible for the acceleration of the expansion of the universe, but
 13 remains even more enigmatic as no explanation can be provided by the Standard Model.

14 Neutrino masses

15 The Standard Model predicts that the neutrinos are massless weakly interacting particles, but obser-
 16 vations by the Sudbury Neutrino Observatory [2] and Super-Kamiokande [3] collaborations show
 17 clear evidence that the neutrinos oscillate from one flavour into another. This can only be explained
 18 if the neutrinos differ in mass, implying that they are not massless and the Standard Model needs
 19 to be extended.

20 2.2 Dark matter

21 One of the current open questions in particle physics that is not answered by the Standard Model is the
 22 existence of dark matter. Many astrophysical observations from gravitational effects (see for instance [4])
 23 show there must be some additional matter in the universe, the so-called dark matter, next to the known
 24 matter. Despite this, its precise nature remains as of yet unknown. Countless theoretical models are being
 25 constructed in order to explain its origin, and on the experimental side dark matter is being looked for in
 26 many different ways, but no observation has been made so far.

27 2.2.1 Observational evidence

28 The first hints of dark matter were observed by F. Zwicky [5] in 1933 by studying the velocity dispersion
 29 of galaxies in the Coma cluster. The effect is not only observed for entire galaxies, but also for various
 30 luminous objects, such as stars or gas clouds, inside a galaxy. The rotation curves of galaxies have been
 31 well studied, and show clear evidence for the existence of dark matter. An example of a rotation curve is
 32 shown in Figure 2.2, exhibiting a flat behaviour at large distances, going even far beyond the edge of the
 33 visible disk.

34 However, in Newtonian dynamics the circular velocity is expected to be

$$v(r) = \sqrt{\frac{GM(r)}{r}}, \quad (2.6)$$

35 where $M(r) = 4\pi \int \rho(r)r^2 dr$ with $\rho(r)$ the mass density profile. The circular velocity is thus expected
 36 to fall like $1/\sqrt{r}$ beyond the disk. Since the measurements show an approximately constant velocity, this
 37 implies the existence of a halo with $M(r) \propto r$ and $\rho(r) \propto 1/r^2$. A universal density profile seems to
 38 be suggested by the rotation curves of both low and high surface luminosity galaxies, consisting of an
 39 exponential thin stellar disk and a spherical dark matter halo with a flat core of radius r_0 and density
 40 $\rho_0 = 4.5 \times 10^{-2}(r_0/kpc)^{-2/3} M_\odot pc^{-3}$ [7]¹.

41 Another evidence for dark matter comes from the effect of gravitational lensing, allowing to determine
 42 the mass of an object regardless of the light it emits. When a distant star or quasar is aligned with a
 43 massive compact object, the bending of its light due to the gravitational field of the massive object can

¹ M_\odot denotes a solar mass, $2 \times 10^{30} \text{ kg}$.

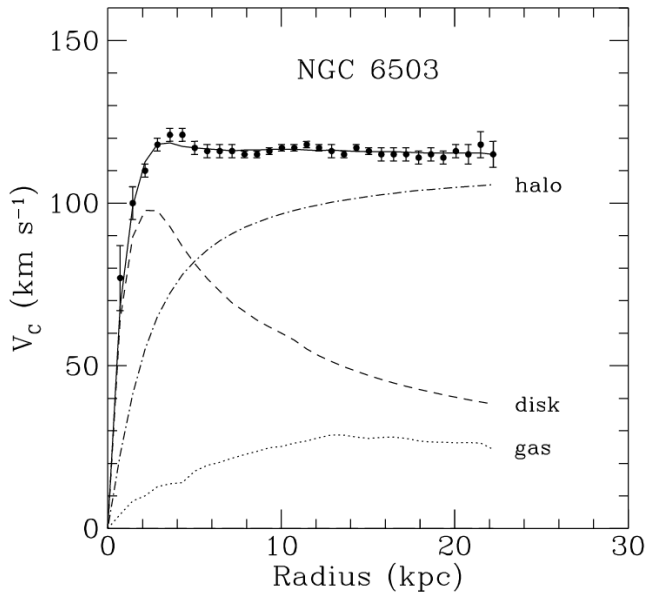


Figure 2.2: Rotation curve of NGC 6503. The dotted, dashed, and dash-dotted lines show the contributions of gas, disk, and dark matter, respectively. Figure taken from [6].

lead to multiple distorted, magnified, and brightened images, as illustrated in Figure 2.3. The distortion of the image can then be used to determine the potential well and thus the mass of the massive object. Yet another way to determine the mass of cluster of galaxies, next to gravitational lensing and the distribution of radial velocities, is by studying the profile of X-ray emission, tracing the distribution of hot emitting gas in rich clusters. In general, these three methods are in reasonable agreement.

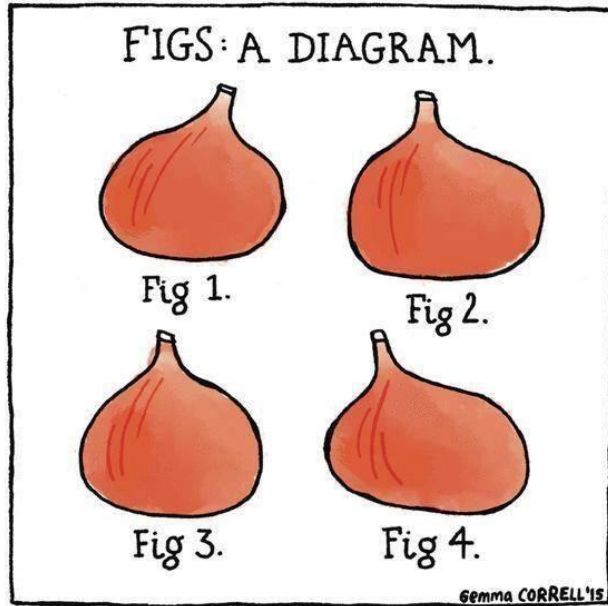


Figure 2.3: TODO

Additionally, at a cosmological level, the analysis of the Cosmic Microwave Background (CMB) allows to determine the total amount of dark matter in the universe. The existence of this isotropic background radiation was already predicted in 1948, and unintentionally discovered by A. Penzias and

R. Wilson in 1965 [8]. This relic radiation comes from the propagation of photons in the early universe, once they decoupled from matter. Before this, the photons were energetic enough to ionise hydrogen, stripping it of its electron and resulting in a plasma. Once the photons cooled down, the hydrogen atoms recombine and the universe became transparent. The photons can then travel freely without scattering off the protons and electrons of the plasma, still carrying information from this surface of last scattering. The CMB is now known to be isotropic at the level of 10^{-5} and to follow the spectrum of a black body corresponding to a temperature of 2.726 K. However, recent results using the WMAP and Planck data show small anisotropies in the CMB as can be seen in Figure 2.4, which correspond to small thermal variations. These anisotropies are usually expanded as

$$\frac{\delta T}{T}(\theta, \phi) = \sum_{l=2}^{+\infty} \sum_{m=-l}^{+l} a_{lm} Y_{lm}(\theta, \phi), \quad (2.7)$$

where $Y_{lm}(\theta, \phi)$ are spherical harmonics. The variance of a_{lm} is given by

$$C_l = \langle |a_{lm}|^2 \rangle = \frac{1}{2l+1} \sum_{m=-l}^{+l} |a_{lm}|. \quad (2.8)$$

As the temperature fluctuations appear to be Gaussian, all the information contained in the CMB anisotropy maps can be condensed into the power spectrum given by the behaviour of C_l as a function of l . This is generally represented using $l(l+1)C_l/2\pi$, as illustrated in Figure 2.5.

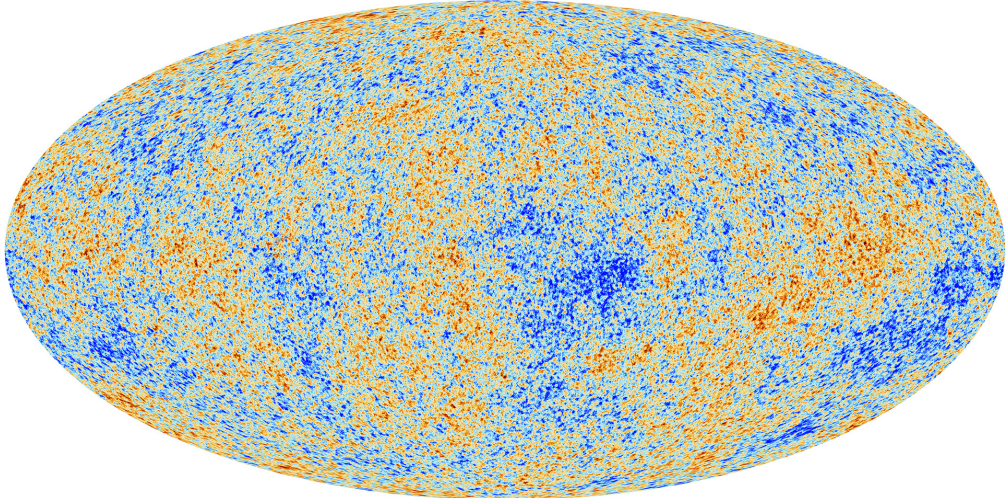


Figure 2.4: The CMB temperature fluctuations obtained from the Planck data.

The CMB anisotropies are caused by acoustic oscillations arising from the conflict between the gravitational pull from baryons and dark matter and the repulsive force due to the radiation pressure from the photons. The angular scale of the first peak can then be used determine the curvature of the universe. The second peak determines the reduced baryon density and the third peak can be used to retrieve information about the dark matter density. From the analysis of the WMAP data the abundance of baryons and matter in the universe is determined to be

$$\Omega_b h^2 = 0.024 \pm 0.0001 \quad \Omega_M h^2 = 0.14 \pm 0.02 \quad (2.9)$$

More evidence for dark matter was found from a great variety of data, both on subgalactic and intergalactic scales. Without discussing them here in detail, a few examples are the velocity dispersions of spiral galaxy satellites, suggesting the existence of dark halos around spiral galaxies extending well beyond the visible disk [9], the velocity dispersion of dwarf spheroidal galaxies, implying larger mass-to-light ratios than those observed in our local neighbourhood [10], and the so-called Oort discrepancy in the disk of the Milky Way, inferring the existence of dark matter from the inconsistency between the amount of stars in the solar neighbourhood and the gravitational potential indicated by their distribution [11].

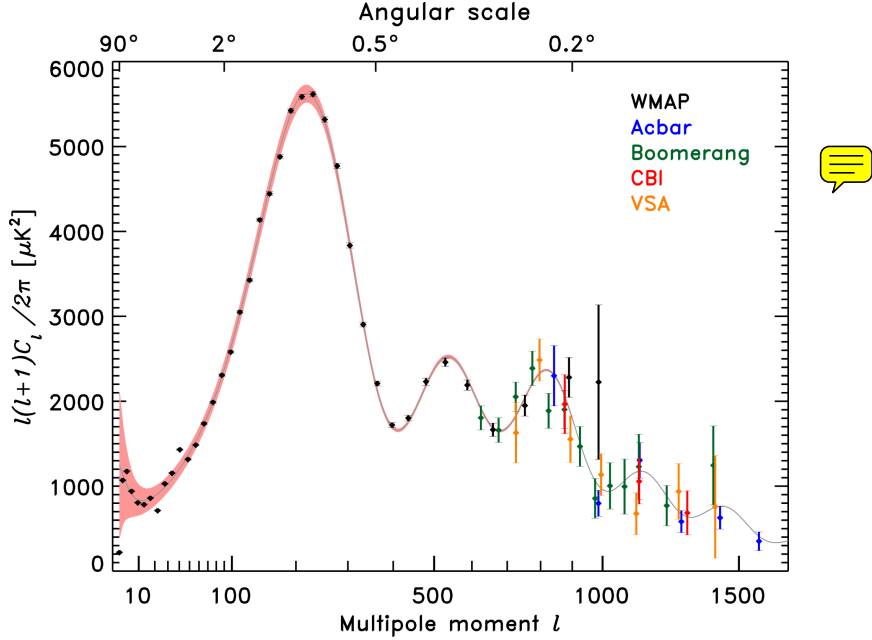


Figure 2.5: The observed power spectrum of the CMB anisotropies.

2.2.2 Dark matter models

Since very little is known so far concerning the nature of dark matter, a multitude of dark matter candidates are discussed in the literature. Without attempting to be complete, a list is given and a few of the more popular candidates are briefly covered here.

Standard Model neutrinos

As mentioned before, the Standard Model could explain the existence of dark matter with the already observed neutrinos. However, it can be shown that their total relic density is predicted to be

$$\Omega_\nu h^2 = \sum_{i=1}^3 \frac{m_i}{93 \text{ eV}}, \quad (2.10)$$

taking the sum over the 3 neutrino flavours. Currently, the most stringent upper bounds on the neutrino mass are

$$m_\nu < 2.05 \text{ eV} \quad \text{at 95% CL} \quad (2.11)$$

obtained in tritium β -decay experiments at Troitsk [12, 13] and Mainz [14]. Since the mass difference between the 3 neutrinos must be very small to explain solar and atmospheric neutrino anomalies [15], this mass limit applies to the three mass eigenvalues, implying an upper bound on the total neutrino relic density of

$$\Omega_\nu h^2 \lesssim 0.07. \quad (2.12)$$

This shows that Standard Model neutrinos are not abundant enough to be the dominant component of dark matter.

Sterile neutrinos

Proposed in 1993 by Dodelson and Widrow [16], these hypothetical particles are similar to the Standard Model neutrinos, but without Standard Model weak interactions, except for mixing. The analysis of their cosmological abundance and the study of their decay products places stringent constraints on the sterile neutrinos. Light neutrinos with masses below a few keV would for example be ruled out.

Axions

These particles were originally introduced to solve the problem of CP-violation, and have often

1 been discussed as dark matter candidates. They are expected to interact extremely weakly with
 2 Standard Model particles. Furthermore, observations from laboratory searches, stellar cooling, and
 3 the dynamics of supernova 1987A constrain the axion mass to be very small, of the order of or
 4 below 0.01 eV.

5 **SUSY candidates**

6 Several particles in supersymmetry (SUSY) models can serve as dark matter candidate, such as
 7 gravitinos and neutralinos. Gravitinos are the superpartners of the graviton. In some SUSY mod-
 8 els, they can be the lightest supersymmetry particle and be stable. While they are very strongly
 9 motivated theoretically, they are very difficult to observe, as they only interact gravitationally. The
 10 neutralinos are the superpartners of the photon, Z boson, and neutral Higgs bosons. The lightest of
 11 the four is stable and is an excellent dark matter candidate. These dark matter candidates are often
 12 called weakly interacting massive particles (WIMPs), since they are massive and interact rather
 13 weakly.

14 In general, WIMPs are hypothetical new elementary particles that interact gravitationally and through
 15 any other force which is as weak or weaker than the Standard Model weak interaction. They should
 16 have been thermally produced in the early universe, and usually constitute cold dark matter. Since SUSY
 17 models predict a new particle with the correct properties and self-annihilation cross section to obtain the
 18 correct abundance of dark matter today, this coincidence is called the “WIMP miracle”. A stable super-
 19 symmetric partner has therefore long been a very plausible dark matter candidate and a lot of experimental
 20 effort has been made to detect WIMPs. **should I write more about WIMPs?**

21 Many more dark matter candidates are discussed in literature, such as but not limited to **to finish**

22 **2.2.3 Detection of dark matter**

23 **TODO**

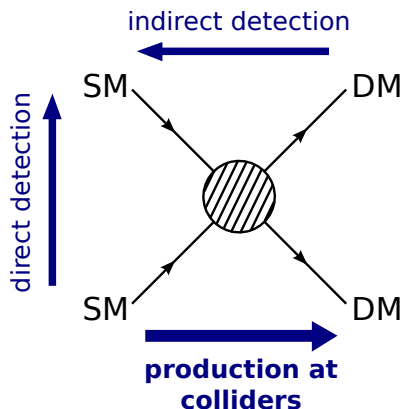


Figure 2.6: .

24 **2.2.3.1 Direct detection experiments**

25 This category of experiments is based on the fact that if our galaxy is filled with WIMPs, then many of
 26 them should pass through the Earth, and they could be detected by looking for the interaction of such
 27 particles with matter. This is for example done by recording the recoil energy of nuclei when WIMPs
 28 scatter off them. In order to determine the expected rate of events per unit detector material mass, the
 29 WIMP-nucleon scattering cross section and the density and velocity distribution of the WIMPs in the
 30 solar neighbourhood are needed.

31 There are several types of scattering processes which can be classified by two relevant characteristics:
 32 elastic or inelastic scattering and spin-dependent or spin-independent scattering. In the case of elastic
 33 scattering, the WIMP simply scatters off a nucleus as a whole, causing it to recoil. The recoil energy

1 spectrum can then be measured by detecting the emitted scintillation light with very sensitive detectors.
 2 Taking a Maxwell-Boltzmann velocity distribution with a characteristic velocity of 270 km/s, the recoil
 3 spectrum is exponential with typical energies of $\langle E \rangle \sim 50$ keV, easily detectable by current experi-
 4 ments, which can detect recoils as low as 1-10 keV. Instead, when the WIMP scatters inelastically, it
 5 interacts with the orbital electrons of the target, exciting the electrons or ionising the target. Differently,
 6 the WIMP could also excite the target nuclei, which would then emit a photon about a nanosecond after
 7 the observed recoil. This signature has, however, to compete with the background from natural radioac-
 8 tivity.

9 The spin dependence or independence of the scattering depends on the coupling of the WIMPs to
 10 the Standard Model particles. Axial-vector or spin-dependent interactions result from couplings to the
 11 spin content of a nucleon, yielding cross sections that are proportional to $J(J+1)$ instead of the number
 12 of nucleons. For scalar or spin-independent interactions, the cross section instead increases considerably
 13 with the mass of the target nuclei. The spin-independent scattering therefore dominates over the spin-
 14 dependent one in experiments which use heavy atoms.

15 Numerous direct detection experiments are currently operational or in development. They use one or
 16 more techniques to measure the nuclear recoil, by detecting the scintillation light, photons, or ionisation.
 17 Some experiments also try to separate the WIMP signatures from the background by looking for an annual
 18 modulation in the rate, which arises due to the Earth's movement around the Sun. This effect causes the
 19 Earth to have a relative velocity with respect to the galaxy's reference frame, given by

$$v_E = 220 \text{ km/s} (1.05 + 0.07 \cos(2\pi(t - t_m))), \quad (2.13)$$

20 where the time is in units of years and t_m is approximately the beginning of June. As a result, a small
 21 variation of about 7% in the WIMP flux can be measured in the direct detection rate.

22 experimental results

23 2.2.3.2 Indirect detection experiments

24 The indirect detection of dark matter is performed by looking for the radiation produced in dark matter
 25 annihilations. The flux of such radiation is proportional to the annihilation rate, which depends on the
 26 square of the dark matter density

27 2.2.3.3 Collider experiments

28 2.3 Strongly Interacting Massive Particles

29 As no observation of dark matter was made, despite many searches probing the more popular models
 30 described in the previous section, many scenarios now venture beyond minimal models or give up basic
 31 assumptions for the WIMP. In the following model, which is studied in this thesis, the interaction cross
 32 section of the dark matter with normal matter is so high that the particles are no longer WIMPs, but
 33 so-called strongly interacting massive particles (SIMPs). This model can also be motivated by the long
 34 lasting interest for self-interacting dark matter (SIDM)² particles with a large cross section [17], which
 35 could help to explain observations that present a challenge for the cold dark matter scenarios, such as
 36 missing satellites or core-cusp problems [18–21]. While it is possible to create models with a strongly
 37 interacting hidden sector that is weakly coupled to the Standard Model particles, it could be just as
 38 reasonable to consider SIDM particles that interact rather strongly with the known matter particles.

39 2.3.1 The SIMP simplified model

40 In this simplified model, the dark matter particles χ can be produced at the LHC in pairs, through a
 41 new strong interaction with a new mediator ϕ , as illustrated in Figure 2.7. These fermionic dark matter
 42 candidates, also called SIMPs, are neutral and stable, and are generated off-shell as the mediator is very

²Incidentally, self-interacting and strongly interacting share the same abbreviation, such that SIDM can also stand for strongly interacting dark matter and SIMP for self-interacting massive particles in the literature.

¹ light, of the order of the pion mass: $m_\phi = 140$ MeV. Both the cases with a scalar or a vector mediator
² can be studied, and the corresponding interaction Lagrangian is

$$\mathcal{L}_{\text{int}} = \quad (2.14)$$

³ with $g_\chi g_q, \tilde{g}_\chi \tilde{g}_q < 0$ to avoid the formation of bound states. For simplicity we assume that the SIMPs have
⁴ a universal coupling to quarks, although a **flavour** dependent coupling could be preferred, as light SIMPs
⁵ with a significant coupling to b or c quarks are probably constrained by B and D meson phenomenology.

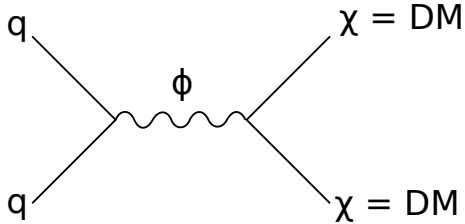


Figure 2.7: Feynman diagram showing the production of a SIMP pair, through a new low-mass mediator.

⁶ Introducing a new strong interaction between quarks is not entirely harmless, as it can modify nuclear
⁷ potentials. In order to keep the impact small, the mediator is assumed to not modify nuclear potentials
⁸ by more than $\mathcal{O}(10\%)$, such that $g_{\chi N} \lesssim 0.3 g_{\pi NN} \sim 3$ for a mediator with the mass of a pion, where
⁹ $g_{\pi NN} \sim 13$ is the effective pseudoscalar pion-nucleon coupling [22]. The quoted values need to be
¹⁰ taken with a grain of salt as a large spread of values can be found in the literature for meson-nucleon
¹¹ effective couplings, sometimes differing by a factor 2 or more (see e.g. [23] for comparison). This shows
¹² the difficulty of dealing with strong interactions in the framework of effective field theories, i.e. in the
¹³ absence of a small parameter. No constraints on modified strong interactions at low energies seem to exist
¹⁴ in literature so far, however searches at fixed-target experiments do place constraints on the existence of
¹⁵ strongly interacting stable neutral particles.

¹⁶ In summary, the model has 4 free parameters: the two couplings, the mass of the mediator m_ϕ , and
¹⁷ the mass of the SIMP m_χ . At the LHC, only the product of the couplings appears, while astrophysical
¹⁸ observations constrain both the dark matter self-interaction and the interaction with the Standard Model.

¹⁹ 2.3.2 Experimental constraints

²⁰ Various types of experiments and observations set constraints on SIMPs as dark matter candidates. How-
²¹ ever, some of these limitations can be avoided by the assumptions in the model described above. The
²² relevant existing measurements are described below, showing there is still a part of phase space which
²³ remained unexplored so far.

²⁴ Bound states

²⁵ Searches for heavy isotopes, in particular heavy water, constrain the formation of bound states
²⁶ between SIMPs and nucleons, ruling out particles with a mass below 10 TeV for the scenario
²⁷ with SIMPs as dominant contribution to dark matter. As mentioned previously, this constraint is
²⁸ evaded by assuming a purely repulsive SIMP-nucleon interaction with opposite sign couplings. In
²⁹ the vector mediator case, vector mediators would however couple to the dark matter antiparticles
³⁰ with an opposite charge. This is avoided if no dark matter antiparticles are around, i.e. if the
³¹ abundance of dark matter is asymmetric. A reason for having asymmetric SIMPs is that if they are
³² the dominant source of dark matter, then the dark matter abundance is set by either an asymmetry
³³ or through a non-thermal mechanism. In the case of a symmetric SIMP candidate, the dark matter
³⁴ abundance is determined by thermal freeze-out, and it can only be a sub-dominant component.
³⁵ Additional constraints also exist on the dark matter self-interacting strength from halo shapes and
³⁶ merging galaxies such as the Bullet cluster [24, 25].

1 **Earth heating**

2 A second argument for an asymmetric abundance of SIMPs comes from experiments measuring the
 3 heat emitted from the Earth's core. For the typical SIMPs cross sections, the dark matter particles
 4 can be captured by the Earth and accumulate in its core over time. Annihilating SIMPs would then
 5 provide a substantial source of heat and could modify the Earth's heat flow. This can be measured
 6 by detectors in deep underground shafts [26] and rules out the scenario with symmetric SIMPs.

7 **Neutron stars and black holes**

8 In the asymmetric scenario, light scalar dark matter particles can however be collected in the cores
 9 of neutron stars and cause them to collapse into black holes. Bosonic dark matter candidates are
 10 therefore excluded, and we consider only fermionic candidates as mentioned previously.

11 **Direct detection searches**

12 Many bounds on the SIMP parameter space also come from the direct detection searches. ~~The~~
 13 ~~underground experiments, such as CDMS and XENON, place strong constraints at slightly smaller~~
 14 ~~cross sections. At the higher cross sections considered here, the SIMPs are stopped by the Earth's~~
 15 ~~atmosphere, and they cannot reach the underground detectors. At higher altitudes however, space~~
 16 ~~or airborne experiments such as RSS [27], a balloon-based experiment with a silicon semicon-~~
 17 ~~ductor detector, and XQC [28], a sounding rocket experiment, exclude SIMPs in some regions of~~
 18 ~~phase space. More details on these constraints can be found in [26], where they have already~~
 19 ~~been extensively reviewed.~~

20 **Nucleosynthesis and cosmic rays**

21 There are also bounds from primordial nucleosynthesis and cosmic rays, reviewed in [29] and [30].
 22 The protons in cosmic rays can scatter off dark matter particles and create neutral pions, which
 23 decay to photons and could be detected in gamma ray telescopes. Although limits have been placed
 24 on dark matter-nucleon interactions [30], these constraints depend on many assumptions and adopt
 25 a form of the dark matter density near the galactic core. Since the considered model describes a
 26 nonstandard form of dark matter with a relatively strong interaction with baryons, these densities
 27 may be considerably different.

28 **CMB and large scale structure**

29 Observations of the CMB anisotropies and the large scale structure power spectrum, including from
 30 the Lyman- α data [31, 32] additionally also place strong constraints on interactions between dark
 31 matter and baryons.

32 **Fixed-target experiments**

33 Finally, a relatively old fixed-target experiment led in 1976 at FNAL with a beam of neutral particles
 34 produced by 300 GeV protons hitting a beryllium target was used to look for massive, strongly
 35 interacting, neutral particles [33]. The mass of the particles was determined using their flight time
 36 and their kinetic energy which was measured in a calorimeter. Neutral particles with a mass larger
 37 than 2 GeV were searched for, in order to discriminate the candidates from the background of
 38 neutrons and lighter hadronic states, up to $m_\chi \lesssim \sqrt{E/2} \approx 12$ GeV, limited by the beam energy
 39 of $E = 300$ GeV. Single particle production was considered, ~~but the results evidently apply to pair~~
 40 ~~production as well~~. The search showed no significant excess above the expected background and
 41 limits were placed on the invariant production cross section per nucleon versus the neutral particle
 42 interaction cross section. As an example, for an interaction cross section of 1 mb, a limit on the
 43 total production cross section of about $2.5 \times 10^{-35} \text{ cm}^2 = 25 \text{ pb}$ is found, and this limit is reported
 44 in the Particle Data Group [34]. Comparing the considered SIMP model to this result by simulating
 45 the pair production at $\sqrt{s} = 25$ GeV, one can conclude that SIMPs between 2 and about 6 GeV are
 46 already excluded by this experiment [35].

3

The LHC and the CMS Detector

In order to investigate the currently unsolved mysteries of particle physics, such as the existence of dark matter, many experiments can be conducted, among other things at particle colliders. The largest particle accelerator in the world is the LHC, located at the European Organization for Nuclear Research (CERN) in Geneva, Switzerland. At this accelerator, protons are being accelerated at energies up to 6.5 TeV, giving rise to a record center-of-mass energy of 13 TeV in the proton collisions. Using data from the collisions generated at the interaction points along the accelerator ring, the Standard Model can be tested in many ways and searches for particles beyond the Standard Model can be performed.

In Section 3.1 more details are given about the LHC and the 4 main experiments situated at the interaction points. In particular, the general-purpose Compact Muon Solenoid (CMS) detector is described in Section 3.2.

3.1 The Large Hadron Collider at CERN

The LHC was built in the already existing Large Electron Positron (LEP) collider tunnel, which was excavated in the 1980's and has a circumference of 27.6 km. Contrary to the LEP collider, the LHC accelerates particles of the same charge, namely protons or lead ions. Much higher luminosities can therefore be reached, since only particles are used and the generation of anti-particles is not needed. This was the limiting factor at the Tevatron, where protons and anti-protons were used. Additionally, at the probed energies the colliding particles are not the protons or ions, but their constituents, which carry a varying fraction of the total momentum. This makes the LHC an ideal instrument for exploration at higher energies, as the collisions naturally cover a wide energy range.

3.1.1 The LHC injector chain

The protons (or lead ions) can not directly be injected in the LHC, but need to be accelerated gradually in several pre-accelerators, as illustrated in Figure 3.1. For the proton beams, the LHC injection chain starts at a bottle of hydrogen, where protons are stripped from the hydrogen atoms and accelerated up to 50 MeV by a linear accelerator (LINAC2). The protons are then transferred to a chain of circular accelerators, starting with the Proton Synchrotron Booster (PSB) which accelerates them to an energy of 1.4 GeV. Next, the protons go through the Proton Synchrotron (PS) and are delivered to the Super Proton Synchrotron (SPS) at an energy of 26 GeV. Finally, the protons are injected in the LHC in opposite direction with an energy of 450 GeV.

The lead ions are first accelerated in a different linear accelerator, LINAC3, before being injected in the Low Energy Ion Ring (LEIR) at an energy of 4.5 MeV per nucleon. Here the ions are accelerated

to an energy of 72 MeV per nucleon, and they then follow the same path as the protons through the PS, where they are accelerated to 5.9 GeV and stripped from the last of their electrons, and the SPS, where they are accelerated to 177 GeV. The record center-of-mass energy for heavy ion collisions at the LHC so far has been 5.02 TeV and 8.16 TeV, for lead-lead (Pb-Pb) and proton-lead (p-Pb) collisions in 2015 and 2016, respectively.

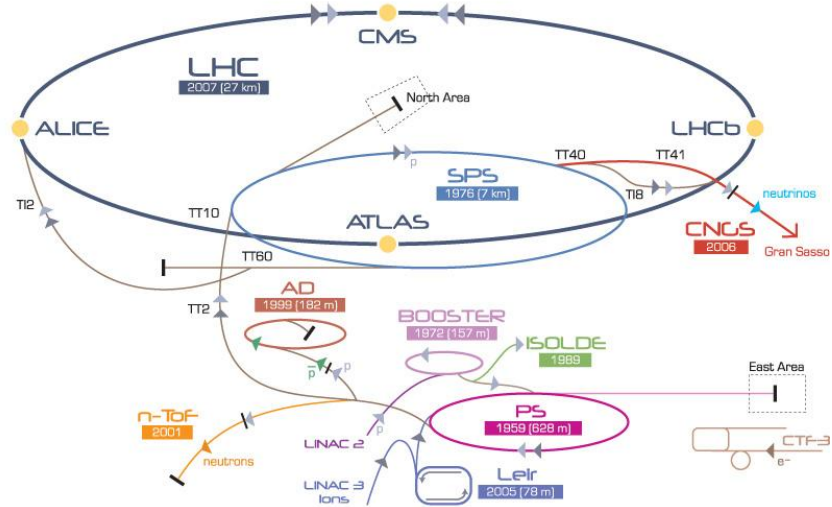


Figure 3.1: Schematic view of the various linear and circular accelerators of the CERN accelerator complex, including the LHC injection chain.

3.1.2 The Large Hadron Collider

The most relevant specifications for a particle physics accelerator are the maximum energy and the luminosity that can be reached. High energy is necessary in order to be able to create new heavy particles, which are for example predicted in many theories beyond the Standard Model.

The protons are kept on the correct orbit by the 1232 LHC dipole magnets. These magnets are cooled down to 1.9 K with liquid Helium and supplied with a current of 12 kA to reach the design field of 8.33 T. This limits the maximum beam momentum of the accelerator to

$$p = B/\rho = 8.33 \text{ T}/2804 \text{ m} = 7 \text{ TeV}/c, \quad (3.1)$$

with ρ the bending radius of the tunnel. The protons are accelerated up to the desired energy by radio-frequency (RF) cavities, which produce an oscillating electric field.

A high event rate or luminosity \mathcal{L} is equally important, to obtain a sufficiently high number of collisions. For a process with cross section σ , this rate is

$$\frac{dN}{dt} = \mathcal{L}\sigma. \quad (3.2)$$

In order to achieve the high design luminosity of $10^{34} \text{ cm}^{-2}\text{s}^{-1}$ in the LHC, the protons are concentrated in bunches with a 25 ns spacing, which are focused by strong quadrupole magnets around the interaction regions. Additionally, 225 ns gaps are present as well between the bunch trains, corresponding to the rise time of the injection kicker magnets. One gap of 3 μs is necessary as well to allow clean beam dumps. These requirements limit the number of bunches to a maximum of 2808.

After almost 25 years of design and construction, the LHC was completed in 2008 and the commissioning of the machine started. However, during a powering test on 19 September of the same year an electric arc developed inside a bus bar which led to a large release of helium and a pressure wave that caused extensive mechanical damage to the affected LHC sector. This incident delayed the first collisions, with one bunch per beam and at a beam energy of 900 GeV, until late 2009. During 2010 and

1 2011 a center-of-mass energy of 7 TeV was used for the collisions, which was then increased to 8 TeV in
 2 2012. The instantaneous luminosity was also increased, starting from $2 \times 10^{32} \text{ cm}^{-2}\text{s}^{-1}$ in 2010 to more
 3 than $6 \times 10^{33} \text{ cm}^{-2}\text{s}^{-1}$ in 2012. During the 3 years of data-taking in Run 1, data corresponding to an
 4 integrated luminosity of 45.0 pb^{-1} , 6.1 fb^{-1} , and 23.3 fb^{-1} , respectively, were delivered. After Run 1, a
 5 long shutdown (LS1) of 2 years followed, which was used to correct the problems that were discovered
 6 in the aftermath of the incident at the startup in 2008, and to upgrade and consolidate the experiments
 7 located on the LHC ring.

8 In 2015, the LHC restarted operations with Run 2, at an even higher center-of-mass energy of 13 TeV.
 9 During 2016 the design luminosity of $10^{34} \text{ cm}^{-2}\text{s}^{-1}$ was exceeded and a total of 41 fb^{-1} of data were
 10 delivered. A comparison of the delivered integrated luminosity per year is shown in Figure 3.2.

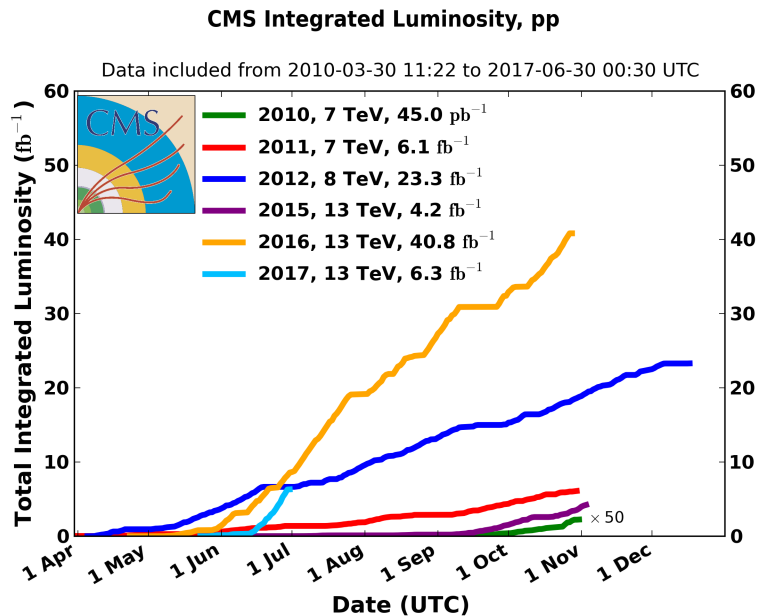


Figure 3.2: Overview of the integrated luminosity delivered to the CMS detector during Run 1 (2010 to 2012) and Run 2 (2015 to 2017).

11 3.1.3 The experiments at the LHC

12 There are four interaction points (IPs) where the proton or lead ion beams of the LHC can collide, and
 13 around each of these points large particle detectors were built in order to record the generated colli-
 14 sions. The ATLAS and CMS detectors, located at IP1 and IP5, are both high luminosity general-purpose
 15 detectors and consist of several layers surrounding the IP in an onion-like structure to avoid particles
 16 escaping detection. These detectors can cover a wide range of high energy physics, from precision mea-
 17 surements of the Standard Model to searches beyond the Standard Model. At IP2 the ALICE detector
 18 is specialized in heavy ion collisions with low instantaneous luminosities, around $10^{27} \text{ cm}^{-2}\text{s}^{-1}$. With
 19 this detector information is gathered about the quark-gluon plasma, a state of matter that exists at ex-
 20 tremely high temperatures and densities where quarks and gluons are no longer confined in hadrons. The
 21 fourth main detector, LHCb, is located at IP8 and requires instantaneous luminosities of the order of a
 22 few $10^{32} \text{ cm}^{-2}\text{s}^{-1}$. Using this detector b quarks are being studied, focusing among other things on the
 23 matter-antimatter asymmetry in the universe.

24 3.2 The CMS detector

25 The searches described in this thesis were conducted using data collected with the CMS detector, a
 26 general-purpose detector located on the LHC ring. It consists of the typical components of a parti-

cle physics detector, namely a tracker, an electromagnetic calorimeter (ECAL), a hadronic calorimeter (HCAL), a solenoidal magnet, and muon detectors. One peculiar aspect is however that both calorimeters are situated inside the superconducting magnet. This design was chosen in order to improve the energy resolution by reducing the amount of material in front of the calorimeters. The overall detector has a length of 21.6 m, a diameter of 14.6 m and a total weight of 12500 t. A schematic overview is shown in Figure 3.3.

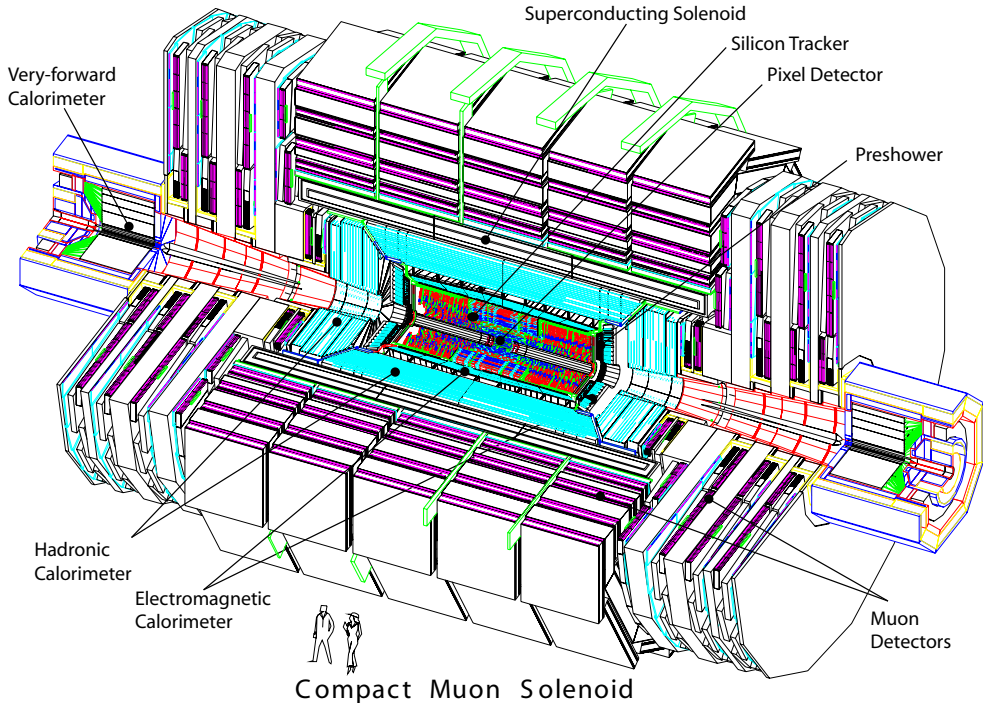


Figure 3.3: The CMS detector, consisting of the pixel and strip tracker; the electromagnetic calorimeter (ECAL) with preshower; the hadronic calorimeter (HCAL) with its forward component, and the muon systems.

The CMS coordinate system places the origin at the nominal collision point. The x axis is perpendicular to the beam and points towards the center of the LHC ring, the y axis is vertical and pointing upwards, and the z axis is defined anti-clockwise along the beam direction. The azimuthal angle ϕ is then defined in the xy plane, relative to the x axis and the polar angle θ is measured with respect to the z axis. In general, the polar angle is converted into the pseudorapidity

$$\eta = -\ln \left(\tan \frac{\theta}{2} \right) \quad (3.3)$$

for convenience, since differences in pseudorapidity are invariant under Lorentz boosts along the z axis. A pseudorapidity of 0 corresponds to the direction perpendicular to the beam ($\theta = \pi/2$), and an infinite pseudorapidity corresponds to the direction parallel to the beam ($\theta = 0$).

Due to the conservation of momentum before and after the collision, the momenta of the particles in the final state of a collision should be balanced in the transverse plane. Another variable that is therefore often used in particle physics is the transverse momentum of a particle, defined as

$$p_T = p \cdot \sin \theta. \quad (3.4)$$

3.2.1 The tracker

The innermost part of the CMS detector, closest to the IP, is the tracking system, which is designed to provide a precise measurement of the trajectories of charged particles. This all-silicon detector is divided into a pixel and a strip detector, with a layout as shown in Figure 3.4. The inner part, consisting of pixel

modules, provides very precise 3D hits, which are important for vertex reconstruction and track seeding. This allows to have a precise measurement of secondary vertices and track impact parameters, necessary for the efficient identification of e.g. heavy flavor particles. As the hit occupancy is lower in the outer part of the detector, a larger cell size can be afforded, and silicon strips are used instead of pixels. This strip detector provides a large lever arm and a link to the calorimeters and the muon system. The tracker covers a pseudorapidity range $|\eta| < 2.5$.

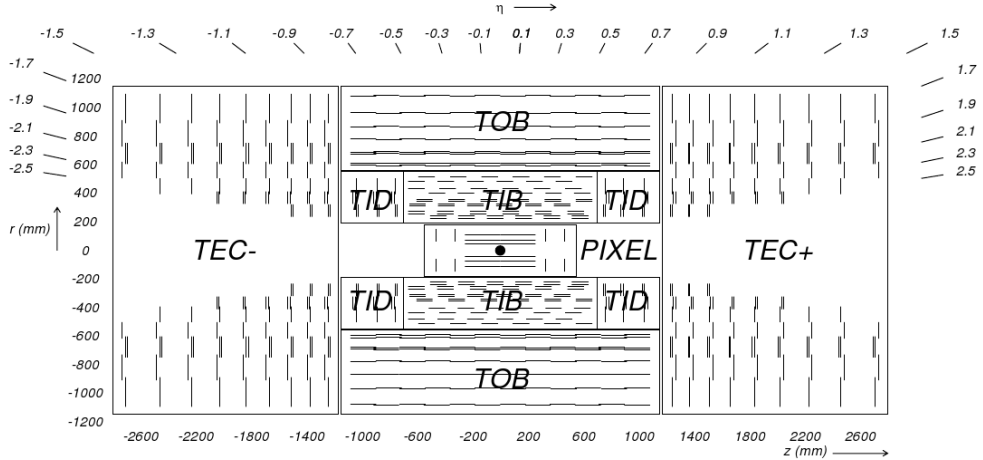


Figure 3.4: A transverse view of the pixel and strip tracker detectors.

3.2.1.1 The pixel tracker

The pixel tracker was replaced during the extended technical stop in 2016 and 2017 [36], as a part of the CMS Phase 1 upgrades. As the data used for this thesis were recorded before that, only the so-called Phase 0 detector is described here.

For the pixel modules n+ pixels on n-substrate are used, allowing the sensors to also work in under-depletion after type inversion. The 1440 modules are arranged in several cylindrical layers and disks, as illustrated in Figure 3.4. The barrel, consisting of 3 pixel layers surrounding the beam pipe at radii of 4.4, 7.3 and 10.2 cm, is complemented by the forward pixel detector, composed of 2 endcap disks on each side extending from 6 to 15 cm in radius. The barrel and the forward parts contain respectively 48 million and 18 million pixels with a size of $100 \times 150 \mu\text{m}^2$, covering a total area of 1.06 m^2 .

In the barrel, the magnetic field of CMS is perpendicular to the drift of the electrons to the collecting pixels, which results in a Lorentz drift. This drift leads to a spread of the charge over several pixels. Since the read-out of the modules is analog, an improved spatial resolution can therefore be achieved with charge interpolation. In the forward pixel detector the drift of the electrons would be parallel to the magnetic field so in order to profit from the Lorentz angle, the modules are tilted by 20° in a turbine-like arrangement, as can be seen in Figure 3.5. A spatial resolution of $10 \mu\text{m}$ ($30 \mu\text{m}$) can be achieved in the local directions x (y) of the module, respectively. In the barrel x is the longitudinal direction perpendicular to the beam and y is the longitudinal direction parallel to the beam.

The signals from the pixel sensors are read out by custom read-out chips (ROCs), which amplify and store the signals, and already apply zero-suppression on-detector. The data rate from the detector to the Front End Drivers (FEDs) is therefore not constant for every event. Additionally, if there are too many hits on a pixel module for a given event, they can not all be stored on the finite buffer of the ROC. Consequently, as the instantaneous luminosity increases the pixel modules start to show a “dynamic inefficiency” which is most pronounced in the first layer, closest to the beampipe. This was one of the main motivations for the Phase 1 upgrade of the pixel detector.

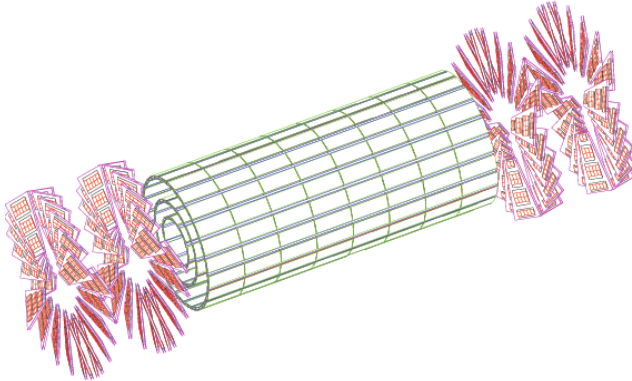


Figure 3.5: A 3D view of the barrel and forward pixel detector.

3.2.1.2 The strip tracker

The outer part of the tracker consists of 15 148 strip modules, which are distributed among multiple barrel layers and endcap disks and make up a total active area of 198 m^2 . The inner part is composed of 4 Tracker Inner Barrel (TIB) layers with 3 Tracker Inner Disks (TID) on each side. Surrounding these are 6 Tracker Outer Barrel (TOB) layers and the 2 Tracker EndCaps (TEC), which are composed of 9 disks. This geometric arrangement is shown in Figure 3.4, with double lines to indicate back-to-back modules. These so-called double-sided modules are mounted with a stereo angle of 100 mrad to improve the 3D point resolution by providing a measurement of the z and r coordinate in the barrel and disks, respectively. The choice of strip pitches is driven by the two particle separation capability and two-hit resolution, and ranges from $80 \mu\text{m}$ to $205 \mu\text{m}$. The length of the strips varies from 63 mm to 117 mm, minimizing the occupancy and noise levels.

In the TOB and the 3 outermost rings of the TEC two silicon sensors are daisy chained, while single sensors are used in the inner part. This is done to limit the number of read-out channels, since the area that had to be instrumented is larger in the outer region. The larger cell size can be afforded due to the lower occupancy in the outer part. However, the noise of the sensors also increases with strip length, so thicker silicon sensors, $500 \mu\text{m}$ compared to $320 \mu\text{m}$ in the inner part, are used in order to collect more signal per traversing particle.

The strip sensors are single sided p-on-n type silicon. The signals from the sensors are amplified, shaped, and stored by 4 or 6 custom APV25 chips per module. When the trigger has made a positive decision, the analog signals from two APV25 chips are multiplexed and sent to the FED boards in the service cavern via optical fibers, where they are converted to digital signals. The FEDs then perform pedestal and common mode subtraction as well as cluster finding. Additionally, the data is sparsified in these off-detector electronics, before being sent to the CMS central data acquisition (DAQ). Due to charge sharing, this analog read-out scheme also results in an improved spatial resolution of 15 to $40 \mu\text{m}$, depending on the position of the modules and the strip pitch.

3.2.2 The electromagnetic calorimeter

Surrounding the tracker, the CMS electromagnetic calorimeter (ECAL) is designed to measure the energy of photons and electrons. It is composed of 75 848 lead tungstate (PbWO_4) crystals arranged in a cylindrical barrel and 2 endcaps. The barrel crystals measure $22 \times 22 \text{ mm}^2$ at the front face of crystal, and $26 \times 26 \text{ mm}^2$ at the rear face, which corresponds to approximately 0.0174×0.0174 in $\eta\phi$. The length of the crystal is 230 mm, corresponding to 25.8 radiation lengths. In the endcaps, the crystals have a rear face cross section of $30 \times 30 \text{ mm}^2$, front face cross section of $28.62 \times 28.62 \text{ mm}^2$, and a length of 220 mm, corresponding to 24.7 radiation lengths.

The high density material was chosen due to its short radiation length and small Moli  re radius, resulting in a small spread of the electromagnetic shower generated by an incoming photon or electron. This allows for a fine granularity, a better shower separation, and a compact calorimeter. Additionally,

1 this scintillating material has a fast response, as about 80% of the light is emitted during the first 25 ns.
 2 The scintillation light is collected by photodetectors, digitized, and read out.

3 The layout of the ECAL is shown in Figure 3.6, with the barrel (EB) extending up to $|\eta| < 1.470$
 4 and the endcaps (EE) on each side covering the range $1.479 < |\eta| < 3.0$. A preshower detector (ES)
 5 is positioned in front of the endcap crystals, covering the pseudorapidity range between $|\eta| = 1.653$
 6 and $|\eta| = 2.6$. This detector consists of a layer of lead which initiates an electromagnetic shower from
 7 incoming photons or electrons, and a layer of silicon sensors which measures the deposited energy. The
 8 main goal of this 20 cm thick detector is to discriminate between photons and neutral pions.

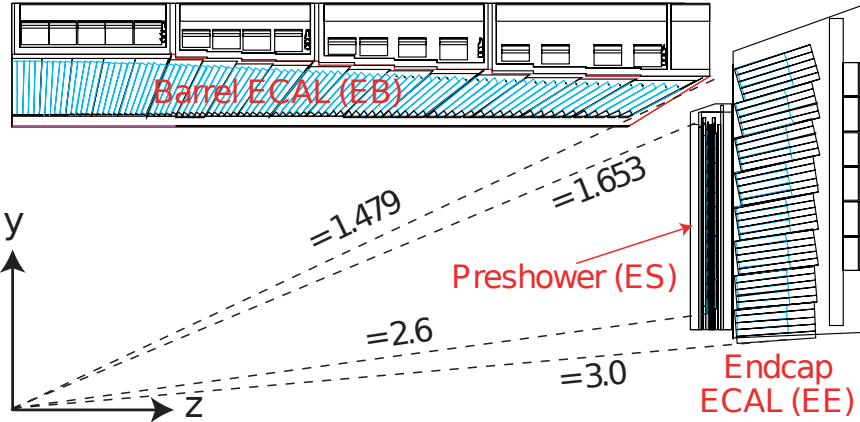


Figure 3.6: A transverse view parallel to the beamline showing one quarter of the ECAL, with its barrel (EB), endcap (EE), and preshower (ES) detectors.

9 The energy resolution of calorimeters can be parametrized by the following stochastic (S), noise (N),
 10 and constant (C) terms:

$$\left(\frac{\sigma}{E}\right)^2 = \left(\frac{S}{\sqrt{E}}\right)^2 + \left(\frac{N}{E}\right)^2 + C^2 \quad (3.5)$$

11 The stochastic term represents contributions from the shower containment, the number of photoelectrons
 12 and the fluctuations in the gain process. The noise term takes into account all noise components, such as
 13 electronics and digitization noise. Finally, the constant term characterizes among others energy leakage
 14 from the back of the calorimeter crystals and non-uniformities of the longitudinal light collection. The
 15 latter term dominates the energy resolution for high-energy electron and photon showers. Figure 3.7
 16 shows the energy dependence of this resolution for incident electrons as measured in a beam test, as well
 17 as the determined stochastic, noise, and constant terms obtained by fitting equation 3.5 to the data.

18 A more recent measurement of the energy resolution was performed using electrons from Z boson
 19 decays in collision data. In the central region, up to $|\eta| < 0.8$, it was measured to be better than 2%. Out-
 20 side of this region, in the more forward direction, the energy resolution is 2-5% [37]. The reconstruction
 21 of the electrons and photons will be discussed in Section 4.3.2.

22 3.2.3 The hadronic calorimeter

23 The hadronic calorimeter (HCAL) surrounds the ECAL with the aim to measure the energy of charged
 24 and neutral hadrons. The missing transverse energy can then be inferred from this measurement together
 25 with the measured energy in the ECAL, in order to identify neutrinos or exotic particles. The HCAL
 26 consists of brass absorber plates interleaved with plastic scintillator tiles.

27 Figure 3.8 shows a longitudinal quarter view of the different HCAL components. A cylindrical barrel
 28 (HB) covers the region up to $|\eta| < 1.4$ and is complemented by endcaps (HE) on each side, extending
 29 the pseudorapidity range to $|\eta| < 3.0$. In the central region, the stopping power of the ECAL and HCAL

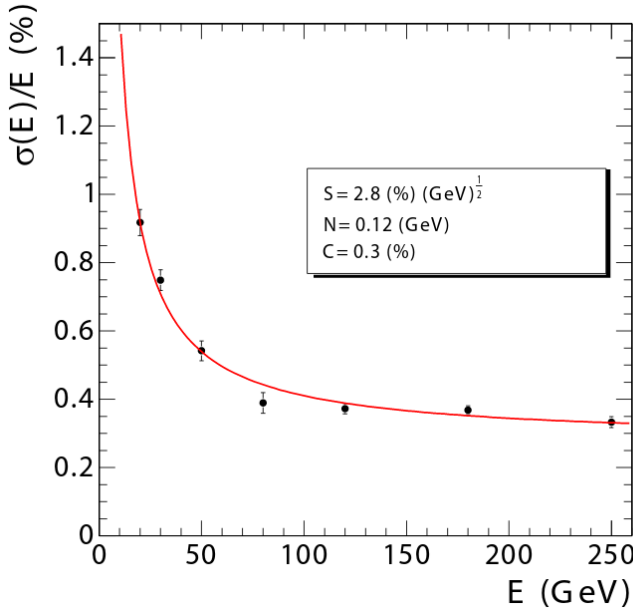


Figure 3.7: The ECAL energy resolution as a function of the electron energy, measured from a beam test. The stochastic (S), noise (N), and constant (C) are given as well.

1 barrel is not sufficient to contain the entire hadron showers. The HCAL was therefore extended outside
 2 the solenoid with an outer calorimeter (HO), which uses the magnet coil as absorber and consists of
 3 scintillators. Two layers are positioned at $\eta = 0$, where the absorber depth is minimal, and only 1 layer is
 4 used for the 2 rings on each side of the central ring. Finally, a forward calorimeter (HF) is positioned at
 5 11.2 m from the IP covering $3.0 < |\eta| < 5.2$. Unlike the other HCAL components, this detector consists
 6 of iron and quartz fibers. Cherenkov-based, radiation-hard technology, since it is exposed to very large
 7 particle fluxes.

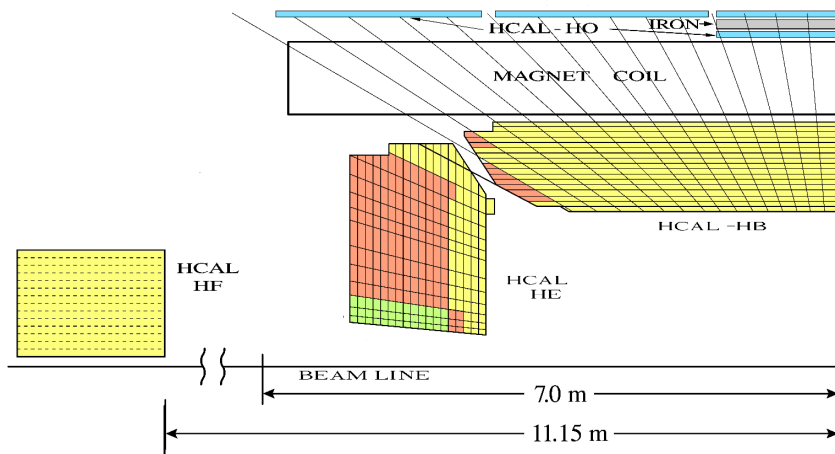


Figure 3.8: A quarter view of the hadronic calorimeter (HCAL), parallel to the beamlne. The barrel (HB), endcap (HE), outer (HO), and forward (HF) detectors are indicated.

8 The optical signals from the scintillators in the HB and HE are converted to electrical signals by
 9 multichannel hybrid photodiodes, while silicon photomultipliers (SiPMs) are used in the HO. In the HF,
 10 the Cherenkov light emitted in the quartz fibers is detected by standard photomultiplier tubes (PMTs),
 11 since the magnetic field is much smaller in this region.
 12 The expected transverse energy resolution for jets is shown in Figure 3.9 for various pseudorapidity

regions: barrel jets ($|\eta| < 1.4$), endcap jets ($1.4 < |\eta| < 3.0$), and very forward jets ($3.0 < |\eta| < 5.0$). Details about the reconstruction of jets from calorimeter and tracking information will be given in Section 4.3.5.

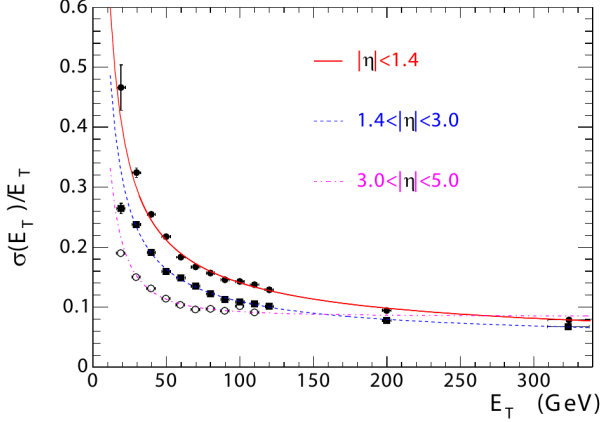


Figure 3.9: The jet transverse energy resolution as a function of the jet transverse energy, for barrel jets ($|\eta| < 1.4$), endcap jets ($1.4 < |\eta| < 3.0$), and very forward jets ($3.0 < |\eta| < 5.0$).

3.2.4 The muon system

The outermost detector, located entirely on the outside of the solenoid, is a dedicated muon detection system. The purpose of this subsystem is muon identification, momentum measurement, and triggering. As illustrated in Figure 3.10, the layers of muon chambers are embedded in the iron yoke constraining the magnetic field lines. The strong magnetic field completely saturates the return yoke with a field of about 2 T, in opposite direction with respect to the field inside the magnet.

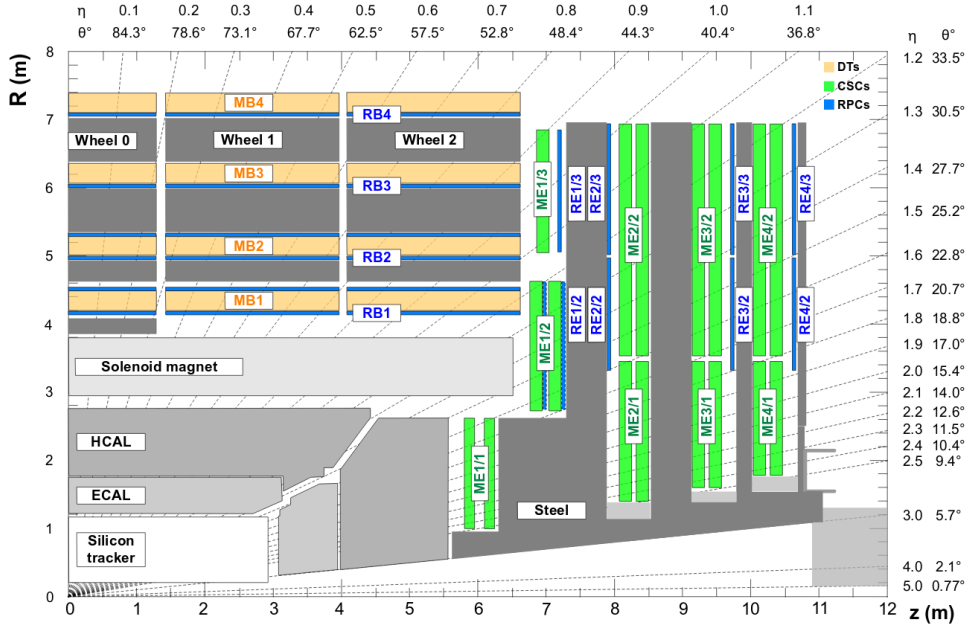


Figure 3.10: A transverse view of one quarter of CMS showing the position of the 3 types of muon detectors. The Drift Tubes (DT) are located in the barrel, the Cathode Strip Chambers (CSC) in the endcaps, and the Resistive Plate Chambers (RPC) in both regions up to $|\eta| < 1.8$.

Three different types of gaseous detectors are used. In the barrel, 4 layers of Drift Tubes (DT) are

installed, covering the pseudorapidity range up to $|\eta| < 1.2$. Due to the higher flux and the larger and non-uniform magnetic field at larger pseudorapidities, Cathode Strip Chambers (CSC) are used in the endcap region ($0.9 < |\eta| < 2.4$). The DTs are designed for the low muon rates that are expected in the barrel and thus have a slower response time than the CSCs. Resistive Plate Chambers (RPCs) complement the DT and CSC systems in the pseudorapidity region up to $|\eta| < 1.8$. They provide a fast response, with a good time resolution but a worse spatial resolution than the DTs or CSCs. The RPCs are therefore very well suited to trigger on muons.

The offline reconstruction efficiency of simulated events containing one muon is typically between 95% and 99%, except for the regions between 2 DT wheels ($|\eta| = 0.25$ and $|\eta| = 0.8$) and the transition region between the DTs and CSCs ($|\eta| = 1.2$), where the efficiency drops to 92%. The reconstruction of muons using the information from the tracker and the muon detectors will be detailed in Section 4.3.3. For low pseudorapidities and small momenta, the offline momentum resolution of the standalone muon system is about 9%. At momenta around 1 TeV, the resolution varies from 15% to 40%, depending on the pseudorapidity. As demonstrated in Figure 3.11, performing a global momentum fit using the tracker as well improves the resolution by an order of magnitude at low muon momenta. At high momenta the resolution of the full system is about 5%.

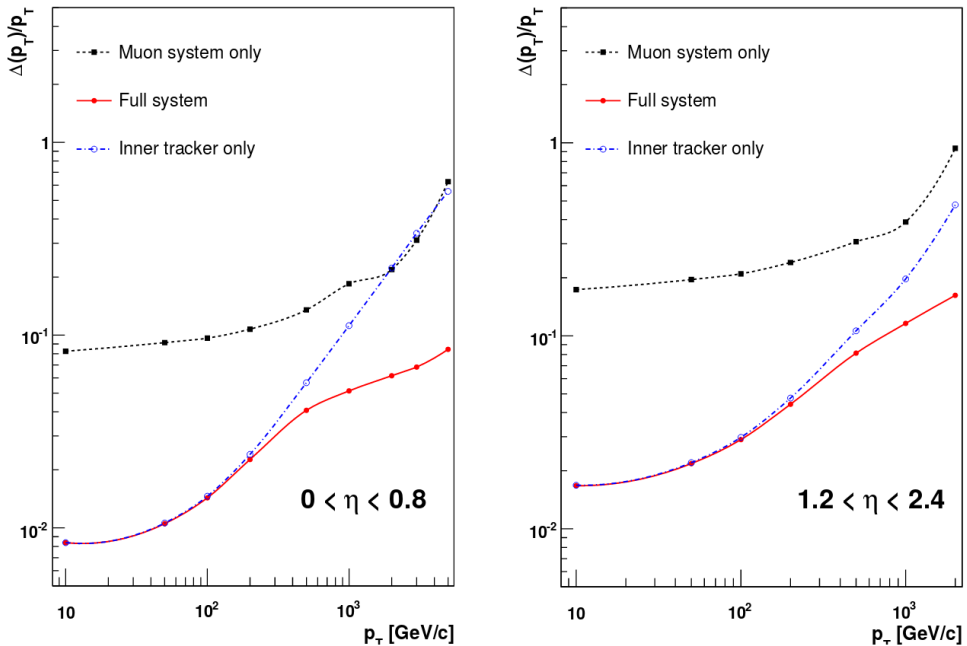


Figure 3.11: The muon transverse momentum resolution as a function of transverse momentum for low (left) and (high) pseudorapidities. The resolution is shown for the muon system and the tracker separately, and for the full system. [38]

3.2.5 Trigger and data acquisition

Collisions are provided by the LHC at high interaction rates, with an interval of 25 ns between bunch crossings. This corresponds to a frequency of 40 MHz. Additionally, multiple collisions occur at the same time, depending on the luminosity. Since it is impossible to store and process the large amount of data produced in the collisions at this high rate, a severe rate reduction is needed. This rate reduction is performed by the trigger system, which decides whether to store or reject an event. Since this decision process is constrained in time, the computing time is optimized by rejecting uninteresting events as quickly as possible. The rate is reduced to 1 kHz in two steps by the Level-1 (L1) Trigger and the High-Level Trigger (HLT).

The L1 Trigger decision is based on information from the calorimeters and muon systems, following the structure illustrated in Figure 3.12. At the lowest level, the Local Triggers are based on energy deposits

in calorimeter towers and track segments or hit patterns in the muon system. Regional triggers, indicated as Calo Trigger Layer 1 and Muon Track-Finder Layer in the figure, then combine this information and use pattern logic to determine trigger objects such as jet or muon candidates in separated spatial regions. The candidates are ranked based on their energy or momentum and quality, reflecting the level of confidence assigned to the L1 parameter measurements. Finally, the Calo Trigger Layer 2 and the Global Muon Trigger (GMT) determine the highest-rank calorimeter and muon objects across the whole detector and transfer them to the Global Trigger, which makes the final decision to accept or reject an event. Following this procedure, the L1 Trigger thresholds are tuned to reduce the event rate to 100 kHz. The L1 Trigger is composed of custom electronics located partially on the detectors, and partially in the underground service cavern. The L1 decision needs to be made and distributed to the detector front-end electronics within 3.8 μ s [39].

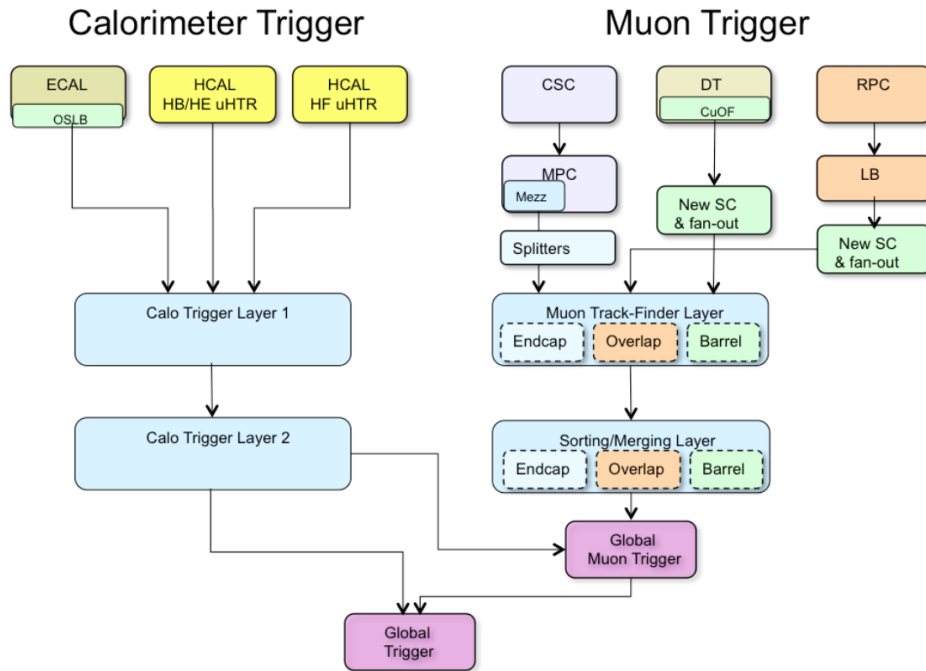


Figure 3.12: Schematic overview of the L1 Trigger. [39]

The readout of the data proceeds as illustrated in Figure 3.13. When an event is accepted by the L1 Trigger, the data from about 740 FEDs is read out by the Readout Units (RUs). For so-called *legacy* systems, i.e. systems which are using VME-based hardware from the initial installation, the FEDs are read out by custom Front-End-Readout-Link (FRL) cards, while for systems that changed their readout architecture from the VME standard to the newer μ TCA standard during or after LS1 they are read out via the newer Front-End-Readout-Optical-Link (FEROL) cards. The event fragments are then sent over the event-builder switch to the Builder Units (BUS), which assemble the events. Next, the events are distributed to the Filter Units (FUs) by a large switch network.

The HLT software system is implemented in this filter farm, which uses more than 15000 CPU cores for the final event selection. In this second step, the HLT reduces the event rate further to 1 kHz. The complete read-out data, including information from the pixel and strip tracker, are available for this step. New objects can therefore be reconstructed such as e.g. tau leptons and b-jets, as is done in the offline software, but speed-optimized.

3.2.6 CMS performance in Run 2

The number of collisions recorded at the experiments will differ from the amount delivered by the LHC. Data loss can be caused by e.g. problems with a particular subdetector, the trigger rate, the data acquisition, or the infrastructure. During Run 2, CMS achieved a data taking efficiency of 89% and 92% in

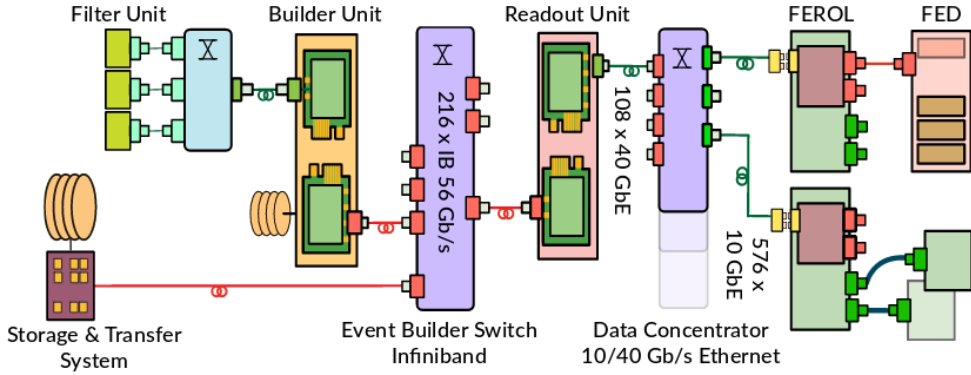


Figure 3.13: Schematic of the data acquisition (DAQ) system. [40]

¹ 2015 and 2016, respectively. The comparison between the delivered and recorded cumulative integrated luminosity in 2016 is shown in Figure 3.14. Subsequently, the recorded data is certified by the offline Data Quality Monitoring (DQM), to ensure that the data are suited for physics analysis.

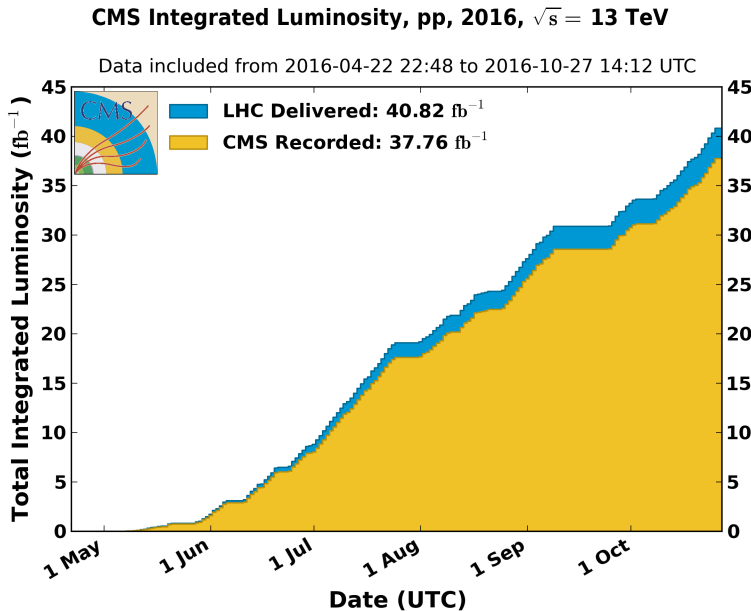


Figure 3.14: The cumulative distribution of the instantaneous luminosity delivered by the LHC (blue) and recorded by CMS (yellow) in 2016.

3.2.6.1 Pre-amplifier saturation in the APV25 chip

⁵ During Run 2, the instantaneous luminosity delivered by the LHC increased continuously, and even exceeded the design luminosity of $10^{34} \text{ cm}^{-2}\text{s}^{-1}$ in 2016. As the luminosity increased, a dynamic inefficiency appeared in the strip tracker, which was most noticeable in the first layer of the TOB. The symptoms were a change in the signal-to-noise ratio and loss of hits. As can be seen from Figure 3.15, the most probable value (MPV) of the signal-to-noise ratio is shifted towards lower values and the low tail increased as well. The loss of hits is clearly visible in Figure 3.16, showing the change in number of hits per track for increasing instantaneous luminosities. The run periods indicated in the plot refer to a subset of the data taken over the course of the year. Run period boundaries are typically defined by changes in the LHC running conditions, changes to the detector configuration or calibration, or other parameters. The number of hits decreases for later run periods such as D and F, as the instantaneous

luminosity increases. This loss of hits results in less and shorter tracks.

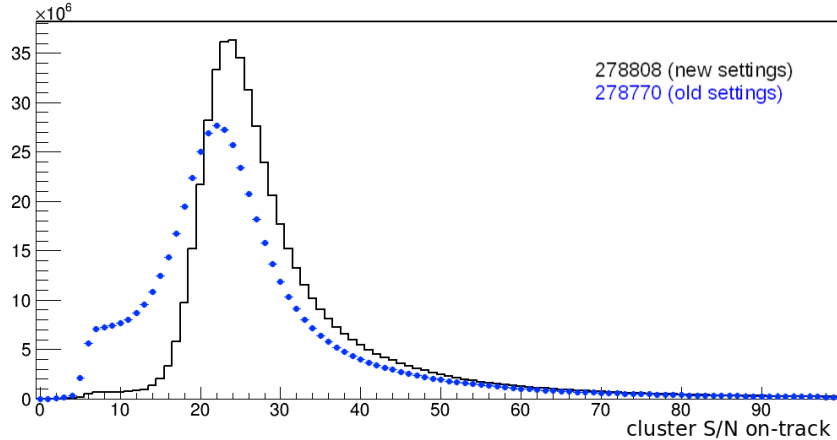


Figure 3.15: The signal-to-noise ratio for clusters on reconstructed tracks in the first layer of the TOB for a run before (blue) and after (black) the change of pre-amplifier drain speed.

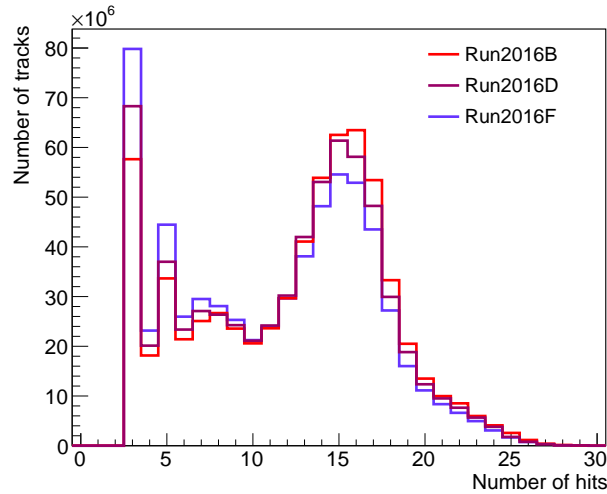


Figure 3.16: The number of hits per track for run periods B, D, and F, showing the effect of the increasing instantaneous luminosity.

The origin of this inefficiency was eventually tracked down to saturation effects in the pre-amplifier of the APV25 chip. The pre-amplifier decay time changes significantly with temperature. As the operating temperature of the strip tracker was lowered from +4°C to -15°C coolant temperature during LS1, the decay time was no longer sufficient to cope with the high luminosities. The dynamic inefficiency was cured in August 2016 by changing the pre-amplifier drain speed. This lead among others to the recovery of the muon efficiency, which showed a large drop for the highest luminosities before the change and an essentially flat behavior afterwards, as demonstrated in Figure 3.17.

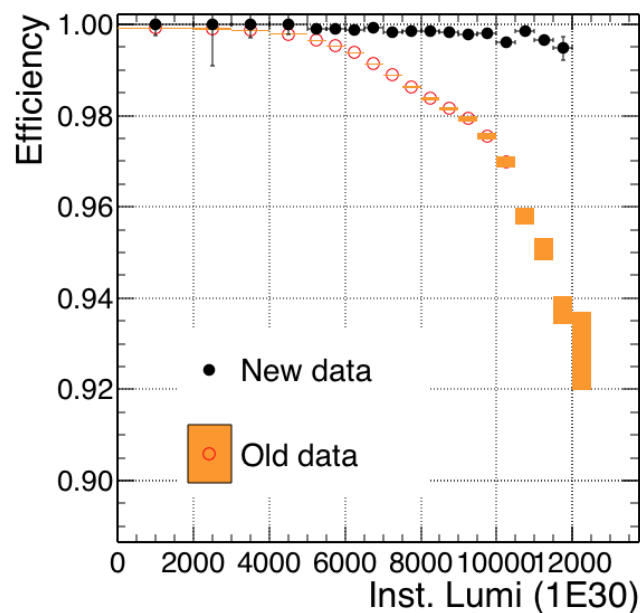


Figure 3.17: The muon efficiency as a function of the instantaneous luminosity for before (orange) and after (black) the change of pre-amplifier drain speed which cured the dynamic inefficiency.

4

1
2

Event Simulation and Reconstruction

3 In order to use the recorded data, the obtained signals coming from various parts of the detector must be
4 reconstructed to be able to identify the particles in the event. Additionally, to compare the experimental
5 results with theory, events are generated and the resulting signals in the detector are simulated, as detailed
6 in Sections 4.1 and 4.2, respectively. The event reconstruction is detailed in Section 4.3. Finally, some
7 details about the simulation of SIMPs are given in Section 4.4.

4.1 Event generation

8 The event structure at the LHC is complicated by the composite nature of protons, as well as the attainable
9 high momentum transfers. A number of aspects must therefore be taken into account when generating
10 events, such as parton distribution functions (PDFs), hard scattering, the parton shower, hadronization,
11 and additional activity in the event.

12 Two partons, meaning the quark or gluon constituents of the colliding protons, will interact with a
13 certain probability for a given momentum transfer. This is parametrized by the PDFs $f(x, Q^2)$, where
14 x is the momentum fraction of the partons and Q^2 is the momentum transfer scale. Experimentally
15 determined PDFs are available from various groups, including e.g. CTEQ [41], MRST/MSTW [42], and
16 NNPDF [43]. An example of such PDFs obtained by the NNPDF group is shown in Figure 4.1. The PDFs
17 are then used to calculate the matrix element of the hard scattering, which is the process of interest where
18 the two colliding partons create high-energetic final state particles. This is done using an event generator,
19 such as MADGRAPH5_aMC@NLO [44] and POWHEG [45]. With MADGRAPH5_aMC@NLO the
20 matrix element can be calculated analytically at tree-level or leading order (LO), and since the addition
21 of aMC@NLO at next-to-leading order (NLO) as well. This generator was used to generate most of
22 the background processes for the Monojet analysis detailed in Chapter 5 and for the SIMP signal used
23 in Chapter 6. POWHEG is able to generate events using NLO computations, but only for a relatively
24 limited number of physics processes. In this thesis, background processes from single-top production
25 were generated with this program. Since NLO calculations are more time-consuming, one can also scale
26 a LO cross section to the NLO level by using a so-called k-factor, defined as the ratio of the NLO and
27 LO cross sections. However, these k-factors often need to be determined as a function of the relevant
28 kinematic variables as they depend on the kinematic phase space and the probed energy scale.

29 Since the colliding partons have a color charge, the hard scattering will be accompanied by a cascade
30 of radiation from QCD processes. This radiation can originate from the incoming partons, which is
31 referred to as initial state radiation (ISR), or the outgoing partons in the final state, the so-called final state
32 radiation (FSR). The perturbative evolution of the cascade can be modeled using the DGLAP (Dokshitzer-
33 Gribov-Lipatov-Altarelli-Parisi) equations [46–48]. These equations describe the time evolution of the

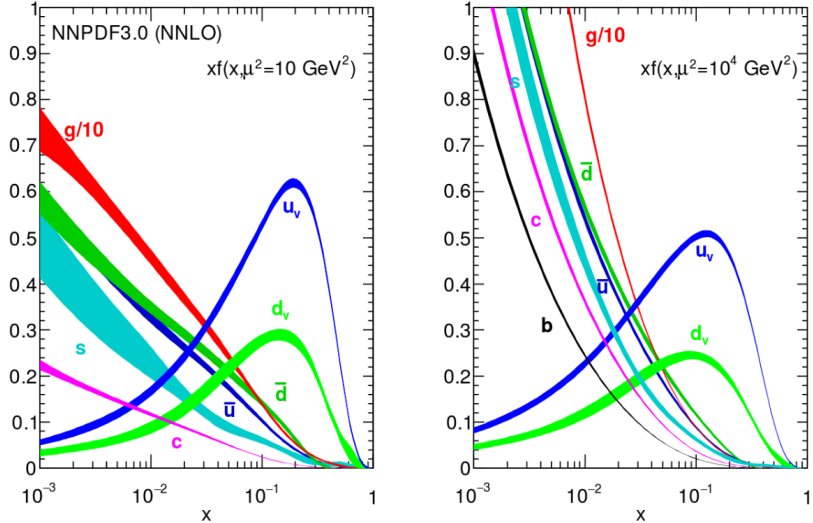


Figure 4.1: The parton distribution functions times the momentum fraction x at energy scales 10 GeV^2 (left) and $10 000 \text{ GeV}^2$ (right), obtained in NNLO NNPDF3.0 global analysis [43].

1 probability of a ‘mother’ parton to split into ‘daughter’ partons at an energy scale Q^2 . The momentum
 2 of the mother is then divided among the daughter partons, which can in turn split into other partons at
 3 a lower Q^2 scale. The cascade continues down to an energy scale Λ_{QCD} where the strong coupling
 4 constant becomes unity.

5 The next step after the showering is the hadronization of the colored particles produced in the parton
 6 shower, transforming them into color-neutral hadrons. Since this happens at low energy scales where the
 7 perturbative approach of QCD is not valid, phenomenological models have to be used. For most of the
 8 processes considered in this thesis, the showering and hadronization is done with PYTHIA 8 [49], using a
 9 standard set of parameters which were tuned to reproduce the experimental data.

10 In addition to ISR and FSR, also beam remnants and multiple parton interactions give rise to ad-
 11 ditional activity in the event, referred to as the underlying event. After the partons participating in the
 12 hard scattering are extracted, the remainder of the protons have a non-zero color charge. The creation of
 13 additional hadrons during the hadronization is therefore possible. Multiple parton interactions represent
 14 additional interactions which can take place between other incoming partons. Finally, additional colli-
 15 sions between other protons in the same bunch crossing or from a previous bunch crossing, respectively
 16 referred to as in-time and out-of-time pileup, add extra activity in the event.

4.2 Detector simulation

18 After being generated, the collision events are passed on to the CMS detector simulation, which is based
 19 on the GEANT 4 [50] simulation toolkit. This toolkit provides a description of the interaction between
 20 particles and the detector material, including effects such as bremsstrahlung of charged particles, photon
 21 conversions, energy loss of charged particles by ionization, and the showering of electrons, photons and
 22 hadrons in the calorimeters due to interaction with the material. The CMS simulation package contains
 23 the geometry of the detector with all the sensitive layers designed to detect the traversing particles, as well
 24 as the dead material regions consisting of e.g. support structures, cables and cooling pipes. A precise map
 25 of the magnetic field is also included in order to simulate the curvature of the charged particles correctly.

26 Next, the electronic response produced by the hits in the active detector material is simulated, resulting
 27 in an event content similar to the output of the real detector. At this point the effect of pileup is also
 28 included by adding detector hits of generated proton-proton interactions on top of the hits resulting from
 29 the main interaction. Most of the simulated event samples used in this thesis are processed using this
 30 detector simulation. However, the interaction of new particles that can arise from specific theory models
 31 is not always readily described in GEANT. This is the case for the signal samples used in the analysis

¹ described in Chapter 6, so an additional step was needed in order to simulate strongly interacting massive
² particles (SIMPs) in the CMS detector.

³ 4.3 Event reconstruction

⁴ Once the detector response has been simulated, the obtained events can be reconstructed. The same
⁵ method is applied for these simulated events and for data coming from the detector. First, the reconstruc-
⁶ tion of tracks is performed, with a specific track reconstruction for electrons and muons. Furthermore,
⁷ the calorimeter deposits, generated by electrons, photons, and hadrons, are grouped into clusters. Addi-
⁸ tionally, the reconstruction is further improved by using the so-called particle flow (PF) algorithm. This
⁹ algorithm greatly improves the performance for jet and hadronic τ decay reconstruction, missing trans-
¹⁰ verse energy momentum determination, as well as electron and muon identification. Finally, the obtained
¹¹ particle flow (PF) candidates are clustered into jets, and the missing transverse energy can be derived.

¹² 4.3.1 Track reconstruction

¹³ The tracks of charged particles going through the CMS tracker are reconstructed with an iterative tracking
¹⁴ approach. This is used to cope with the high occupancy and consequently high combinatorics. Addition-
¹⁵ ally, the first iterations search for tracks with less possible combinations, such as tracks with many pixel
¹⁶ hits or a high momentum. After every iteration, the hits associated with the found track are removed to
¹⁷ reduce the combinatorics. Each iteration consists of four steps:

- ¹⁸ 1. **Seed generation.** In this first step hits are combined into seeds for the subsequent track finding. In
¹⁹ the initial iterations pixel triplets are used, then pixel pairs, in order to take gaps or non-working
²⁰ modules into account. Next, mixed pixel/strip triplets are taken, and finally strip-only seeds are
²¹ used. These additional iterations improve the acceptance in p_T and in displacement with respect to
²² the primary vertex.
- ²³ 2. **Track finding.** The seeds are used as starting point for a Kalman filter algorithm. This method
²⁴ extrapolates the seed trajectory outward to the next layer, taking into account potential energy
²⁵ loss and multiple scattering. If compatible hits are found in the next layer, the parameters of the
²⁶ trajectory are updated. This process continues until the outermost layer of the tracking system.
²⁷ Using this method, a given seed can generate multiple tracks, or different tracks can share hits. A
²⁸ trajectory cleaner therefore determines the fraction of hits the tracks have in common and discards
²⁹ the track with the lowest number of hits when there are too many shared hits. If both tracks have
³⁰ the same number of hits, the track with the largest χ^2 value is removed.
- ³¹ 3. **Track fitting.** The track parameters are then refitted using a Kalman filter and smoother, taking all
³² hits determined in the track finding step into account.
- ³³ 4. **Track selection.** Finally, the tracks are selected based on quality requirements, such as the number
³⁴ of layers that have hits, the χ^2/dof , and the distance to a primary vertex. This greatly reduces the
³⁵ fraction of reconstructed tracks that are fake.

³⁶ The performance of the track reconstruction is excellent, and a high track-finding efficiency is ob-
³⁷ tained [51] while keeping the rate of fake tracks negligible. The highest tracking efficiency is obtained
³⁸ for muons, which traverse the full detector volume and have an improved momentum resolution due to
³⁹ tracking information from the muon detectors giving a long lever arm. For isolated muons with p_T be-
⁴⁰ tween 1 and 100 GeV the tracking efficiency is higher than 99% for the entire η coverage of the tracker,
⁴¹ as can be seen from the left plot in Figure 4.2. The p_T resolution is about 2-3% for a muon with $p_T =$
⁴² 100 GeV up to $|\eta| < 1.6$, but worsens for higher pseudorapidities. Different types of particles interact
⁴³ differently with the detector material. Charged hadrons, for example, are also subject to elastic and in-
⁴⁴ elastic nuclear interactions and have a tracking efficiency of 80-95% depending on pseudorapidity and
⁴⁵ transverse momentum, as shown in the right plot of Figure 4.2.

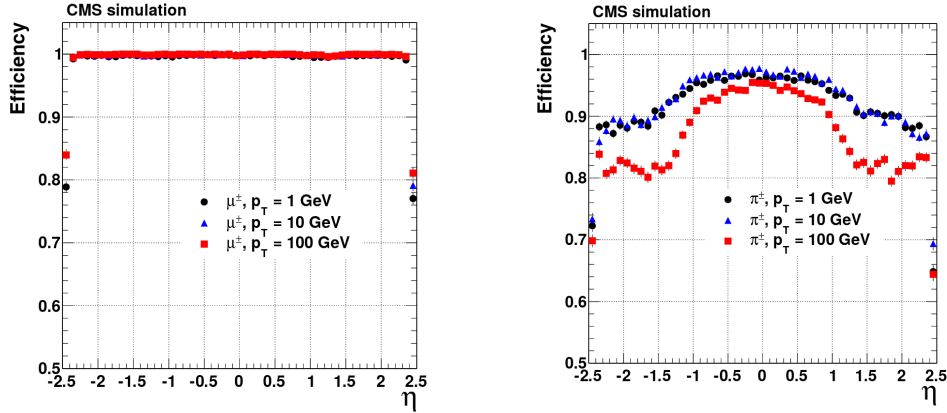


Figure 4.2: The muon efficiency (left) and pion efficiency (right) as a function of pseudorapidity, for multiple transverse momenta. [51]

Finally, the primary vertex is reconstructed from the tracks. Since the collisions happen between bunches of protons, multiple protons will be colliding at the same time. The extra collisions, next to the potentially interesting collision, are referred to as pile-up interactions. The particles generated in these collisions are all detected simultaneously and form a challenge to disentangle them from the particles coming from the to be studied interaction.

The reconstruction is done in 2 steps: first the tracks that appear to originate from the same interaction vertex are clustered, then a fitting procedure computes the vertex parameters and assigns a weight to each associated track, reflecting the probability that it corresponds to the considered vertex. Figure 4.3 shows the reconstruction efficiency and the resolution of the primary vertex. The more tracks, the better the vertex is constrained and thus the better the resolution.

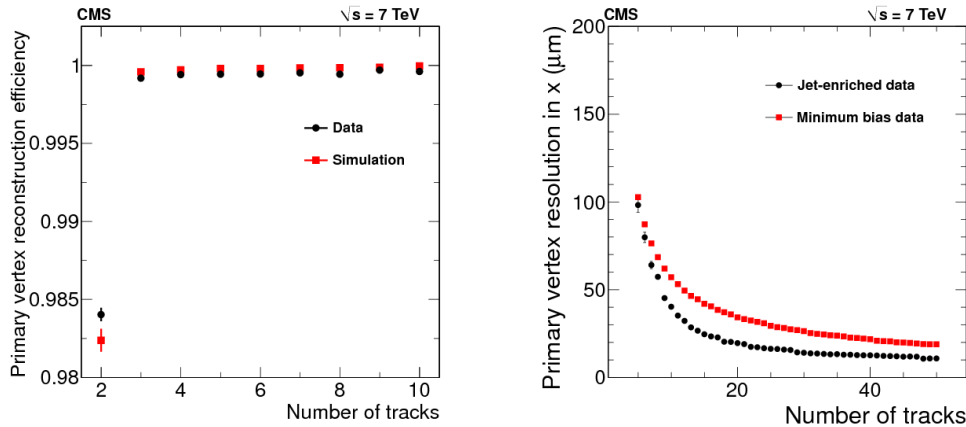


Figure 4.3: The primary vertex reconstruction efficiency (left) and resolution (right) as a function of the number of tracks associated to it. [51]

4.3.2 Electron and isolated photon reconstruction

Electrons are reconstructed using information from both the tracker and the calorimeters. Due to the large amount of material present in the tracker, electrons will emit bremsstrahlung photons, and photons will often convert into e^+e^- pairs, which can again radiate bremsstrahlung photons. The electron and photon reconstruction is therefore very similar.

For electrons, a Gaussian-sum filter (GSF) [52] candidate is taken as starting point. This GSF candidate is obtained using 2 different methods to reconstruct the electron track from the hits in the tracker, which should gather all radiated energy from the electron. First, the ECAL-based approach is used,

grouping ECAL clusters into superclusters. These superclusters collect the energy of the electron and the bremsstrahlung photons in a small η window and a large ϕ window, taking the bending of the electron track in the magnetic field into account. The supercluster energy and position is then used to estimate the position of the corresponding hits in the tracker layers. Subsequently, the tracker-based approach is used to reconstruct electrons missed by the ECAL-based method. In this case, all the tracks from the iterative tracking with transverse momentum larger than 2 GeV are used. Next, the specific electron tracking is performed, using a GSF fit, which is more adapted to electrons than the Kalman filter used in the iterative tracking, as it describes the energy loss in each tracker layer. The electron seeds obtained with both methods are merged and used as input for the full electron tracking, which is performed with twelve GSF components. The obtained electron tracks are then linked to ECAL clusters by the PF algorithm, as described in Section 4.3.4. In the case of isolated photons, a candidate is seeded from an ECAL supercluster with transverse energy larger than 10 GeV which is not linked to a GSF track.

The total energy of the accumulated ECAL clusters is corrected for the energy that was lost in the process of reconstruction, using analytical functions of the energy and pseudorapidity. The applied corrections can be as large as 25%, at low transverse momentum and at $|\eta| = 1.5$, where the material density in the tracker is largest. The energy of the electron is then obtained from a combination of the corrected energy and the momentum of the GSF track, while the direction of the electron is taken from the GSF track. For photons, the corrected energy and the direction of the supercluster are used.

Additionally, the electron and photon candidates must satisfy identification criteria to be retained. In the case of electrons a boosted decision tree is used, combining fourteen variables including the amount of energy radiated and the ratio between the energies gathered in HCAL and ECAL, while for photons the candidates must be isolated from other tracks and calorimeter clusters, and the energy distribution in the ECAL and the ratio between the HCAL and ECAL energies must be compatible with the expectation from a photon shower.

4.3.3 Muon reconstruction

Muon tracking is performed using 2 complementary approaches. The first method starts from standalone muons which are reconstructed from hits in the muon detectors using pattern recognition. The standalone muons are then matched to tracks in the tracker, and the hits are combined to form a global muon track. This global muon fit improves the momentum resolution compared to the tracker-only fit at muon momenta larger than 200 GeV.

For momenta below 10 GeV, muons often fail the global muon conditions which require the muon to penetrate through more than one muon detector plane, due to the large multiple scattering in the return yoke. In this case, tracker muon reconstruction is more efficient since it only requires one muon segment. Each track in the tracker with a transverse momentum larger than 0.5 GeV and a total momentum larger than 2.5 GeV is therefore extrapolated to the muon system and if at least one matching track segment is found, it is retained as muon candidate.

Within the geometrical acceptance of the muon system about 99% of the muons are reconstructed, either as global muon or as tracker muon and frequently as both. Global and tracker muons that share the same track inside the tracker are merged into a single candidate. Muons that are only reconstructed as standalone muons have a worse momentum resolution compared to the global and tracker muons.

Charged hadrons can be misreconstructed as muons if e.g. a part of the hadron shower reaches the muon system. In order to improve the muon identification, the PF muon identification algorithm described in Section 4.3.4 also matches energy deposits in the ECAL and HCAL with the muon track.

4.3.4 Particle flow

The particle flow (PF) algorithm reconstructs so-called particle flow candidates by combining information from all different CMS subdetectors, linking different elements, such as tracks in the tracker, calorimeter clusters, and muon tracks. The obtained collection of particle candidates is subsequently used to reconstruct jets and to determine the missing transverse energy.

In a first step, the PF algorithm identifies charged particle tracks, as defined in Section 4.3.1, and Sections 4.3.2 and 4.3.3 for electron and muon tracks, respectively. At the same time, the calorimeter clusters are reconstructed with a clustering algorithm designed specifically for the PF event reconstruction. In this algorithm, cluster seeds are first identified as local energy maxima with respect to the four or eight closest cells, if the energy deposited in the cell is above a given seed threshold. The clusters are then formed by accumulating neighboring cells with an energy above a given cell threshold, suppressing noise.

The PF elements in the different subdetectors are then connected by a link algorithm which avoids any double counting. The link algorithm produces blocks of associated elements, quantifying the quality of the link by defining a geometrical distance between the elements. When an element is linked to multiple other elements, only the link with the shortest distance is kept. More precisely, a link between a track in the tracker and a calorimeter cluster is made by extrapolating it from the last hit in the tracker to the calorimeters. The distance between the position of the extrapolated track and the cluster in the (η, ϕ) plane is then used to define the link distance. At the interaction points between the track and the tracker layers, tangents to the GSF tracks are extrapolated to the ECAL in order to collect the energy of photons radiated by electron bremsstrahlung. A dedicated conversion finder was also developed to identify bremsstrahlung and prompt photon conversions into e^+e^- pairs. Links between calorimeter clusters are established outside of the tracker acceptance, or between the preshower and ECAL clusters in the preshower acceptance. In this case the link distance is also defined as the distance between the position of the clusters. Charged particle tracks can also be linked by a common secondary vertex. Finally, the PF muon identification algorithm associates the muon tracks to the muon energy deposits in the ECAL and HCAL, to improve the muon identification performance.

In a next step, the PF blocks are classified as muons, electrons, or isolated photons. The corresponding elements are then excluded from further consideration. Once electrons, muons, and isolated photons have been identified, the remaining elements are identified as charged hadrons, neutral hadrons, or photons produced in jets. Within the tracker acceptance, the ECAL clusters not linked to any track are classified as photons, while the clusters in the HCAL without a matched track are labeled as neutral hadrons. Outside of the tracker acceptance, charged and neutral hadrons can not be distinguished. ECAL clusters linked to an HCAL cluster are then assumed to arise from the same hadron shower, and the estimated energy for these particles is the sum of the energy deposited in the ECAL and the HCAL. The remaining clusters are then linked to one or several tracks in order to reconstruct the charged hadrons.

4.3.5 Jet reconstruction

Jets are reconstructed with the anti- k_T algorithm [53], which clusters either the particles reconstructed by the PF algorithm (PF jets) or the energy deposits in the calorimeters (Calo jets). This procedure takes into account the transverse momentum p_T , also called k_T , of the particles and the distance between particles, defined as

$$\Delta R_{ij} = \sqrt{(\eta_i - \eta_j)^2 + (\phi_i - \phi_j)^2}. \quad (4.1)$$

The strategy consists of the following steps:

1. For every pair of particles i and j , a distance d_{ij} defined as

$$d_{ij} = \min \left(\frac{1}{p_{Ti}^2}, \frac{1}{p_{Tj}^2} \right) \frac{\Delta R_{ij}^2}{R^2} \quad (4.2)$$

is calculated.

2. For every particle i , a distance d_{iB} to the beam pipe is calculated with

$$d_{iB} = 1/p_{Ti}^2. \quad (4.3)$$

3. The minimum of d_{ij} and d_{iB} is then determined.

4. If it is d_{ij} , particles i and j are recombined into a new particle by adding the four-momenta of the particles. If it is d_{iB} , particle i is declared to be a jet and it is removed from the list of particles.

1 5. This is repeated until no particles remain.

2 In this clustering algorithm, the parameter R determines what is called a jet. If a particle i has
3 no other particles within a distance R , d_{iB} will be smaller than d_{ij} and the particle will become a jet.
4 A consequence of this is that an arbitrarily soft particle can become a jet, and therefore a minimum
5 transverse momentum for a jet to be of interest is defined.

6 The anti- k_T algorithm favors clustering around hard particles, and the jets then grows outward from
7 this seed. However, since it still involves a combination of energy and angle in the distance measure, this
8 is a collinear-safe growth, meaning that the jet will not change when one of the particles of the jet is split
9 collinearly. This algorithm is also infrared-safe, i.e. the same set of jets is obtained when soft particles
10 are emitted. and gives rise to circular jets.

11 A reliable determination of the jet energy is however not straightforward, since many effects can dis-
12 tort the energy estimation, such as the calorimeter response, the limited particle reconstruction efficiency,
13 the underlying event, the pileup, and the charged particles bending out of the jet cone due to the strong
14 magnetic field. The pileup is mitigated by applying charged hadron subtraction (CHS), which consists of
15 removing charged hadrons associated with vertices other than the primary vertex from the list of PF can-
16 didates. Additionally, the jet energy is corrected using a factorized approach, as illustrated in Figure 4.4,
17 with the following steps:

- 18 • **Pileup correction (L1).** The first level of jet energy corrections is applied event-by-event and jet-
19 by-jet, and is determined from simulation. It is dependent on the pseudorapidity and transverse
20 momentum of the jet, the average p_T density in the event, and the effective jet area. This effective
21 area is determined by injecting a large number of very soft particles in the event before the jet
22 clustering. The spread of the soft particles in each jet then defines the jet area.
- 23 • **Relative η and absolute p_T corrections (L2L3).** This correction is also obtained from simulations
24 and corrects for the non-uniform response of the calorimeters in η and p_T .
- 25 • **Residual η and p_T corrections (L2L3Residual).** Since the L2L3 correction is derived from simu-
26 lation, additional residual corrections are needed in order to correct for the remaining small differ-
27 ences between the jet response in data and simulation. These corrections are typically of the order
28 of a few percent.

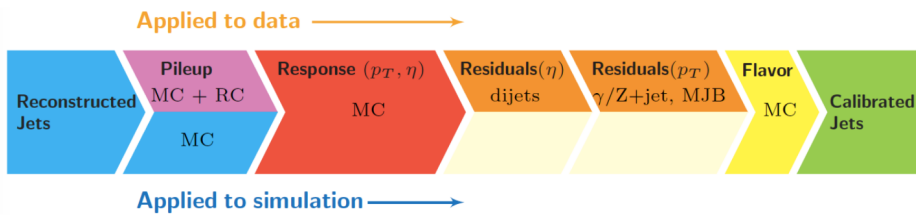


Figure 4.4: Graphical overview of the factorized approach used at CMS to apply jet energy corrections.

29 Finally, a set of identification criteria are applied on the PF jets. A jet is required to consist of at least
30 two particles. For jets in the region $|\eta| < 2.7$, the fraction of energy coming from ether neutral hadrons
31 or photons should not exceed 99%. Additionally, for jets restricted to the tracker acceptance ($|\eta| < 2.4$),
32 there should at least be some energy deposited in the HCAL, the jet should contain 1 or more charged
33 constituent, and the fraction of energy corresponding to electrons or photons should not exceed 99%.

34 4.3.6 Missing transverse energy reconstruction

35 While most particles produced in the collisions can be reconstructed from the hits and energy deposits
36 in the detector, some collision products might not leave energy deposits in tracker, calorimeters or muon
37 system. This makes an accurate reconstruction of this type of particles rather challenging. Another
38 method is therefore used, based on indirect observations. As the detector is hermetically closed such that
39 all other particles in the event can be detected, the missing transverse energy can be determined. This

1 energy then corresponds to all undetected particles in the event, and can be calculated from the vectorial
 2 sum of the transverse momenta of all the observed final state particles:

$$\vec{E}_T^{miss} = - \sum \vec{p}_T, \quad (4.4)$$

3 where the sum runs over all reconstructed PF particles.

4 A notable example of particles leaving no hits or energy deposits behind are neutrinos, as they are
 5 neutral and weakly interacting and will therefore traverse the entire detector. Other hypothetical neutral
 6 weakly interacting particles, which are being searched for in many physics analyses, would escape the
 7 detector without producing hits as well.

8 4.4 Simulation of the SIMP signal

9 For the generation of the SIMP signal, the model Lagrangian given in equation ?? is implemented in
 10 FEYNRULES 2.0 [54]. Next, the matrix element is calculated at LO and events are generated using
 11 MADGRAPH 5. The subsequent parton shower and hadronization is done with PYTHIA 8, using tune
 12 CUEP8M1. Next, the events are simulated in the CMS detector using GEANT. However, the SIMPs
 13 are not included in the simulation, as their interaction with matter is not implemented in GEANT. The
 14 SIMPs were instead incorporated by adding an additional step to the standard reconstruction described in
 15 Section 4.3. In this additional step the SIMPs are directly converted to neutral PF candidates and merged
 16 with the rest of the PF candidates. The standard pileup corrections, jet clustering, and charged hadron
 17 subtraction are then applied in order to obtain the resulting jets, denoted here as P2PF jets.

18 In order to validate this method, a second sample was produced using neutrons instead of SIMPs and
 19 applying the same additional step. In this case the the neutrons will also be correctly reconstructed by the
 20 standard reconstruction. The reconstructed PF candidates that are matched to the generated neutrons were
 21 therefore removed before injecting the converted generated neutrons to the collection of PF candidates.
 22 This sample is then used to evaluate the difference with a standard neutron sample where the full GEANT
 23 simulation is done. Neutrons were chosen because of their resemblance to the SIMPs as single neutral
 24 particles generating a hadronic shower.

25 The two leading generator-level jets (GEN) can then be compared to the uncorrected P2PF jets from
 26 the custom sample and the PF jets from the standard sample. The transverse momentum of these jets is
 27 compared in Figure 4.5. This shows that the jet energy resolution (JER) is not described properly, since
 28 the additional step directly converts generated particles to PF candidates without taking into account any
 29 other effects. In order to produce a more realistic simulation, the new PF candidates are therefore smeared
 30 with JER distributions derived using the uncorrected PF jets matching the neutrons in the standard neutron
 31 sample in bins of η and p_T . An example of this resolution is shown in Figure 4.6 for central neutrons
 32 with low and high transverse momentum.

33 After applying this smearing, the P2PF jets are processed with the standard sequence of charged
 34 hadron subtraction, jet clustering, L1FastJet, and L2/L3 corrections. The comparison of the corrected
 35 P2PF jets and the standard corrected PF jets is shown in Figure 4.7 for the neutron sample, validating
 36 that the jet transverse momentum is now correctly smeared. The JER distributions are also compared in
 37 Figure 4.8 and fitted with a Crystal Ball function, showing compatible parameters. This demonstrates
 38 that the procedure, where the JER distributions derived from a neutron sample are used to smear the PF
 39 candidates from generator-level SIMPs, can sufficiently accurately simulate SIMPs in a realistic detector.

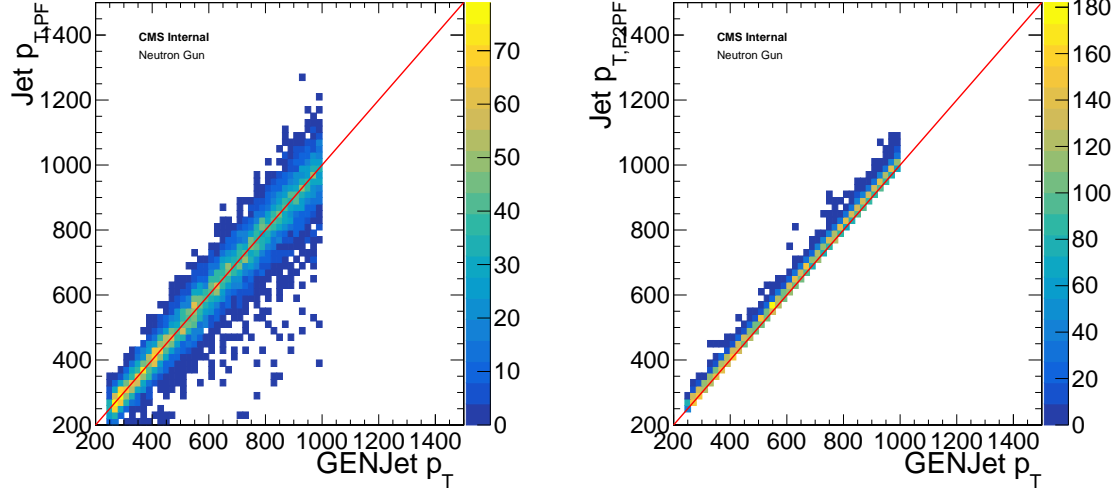


Figure 4.5: Comparison of the transverse momentum of the generator-level jets to the PF jets (left) and P2PF jets (right) without jet energy resolution smearing, using a neutron sample.

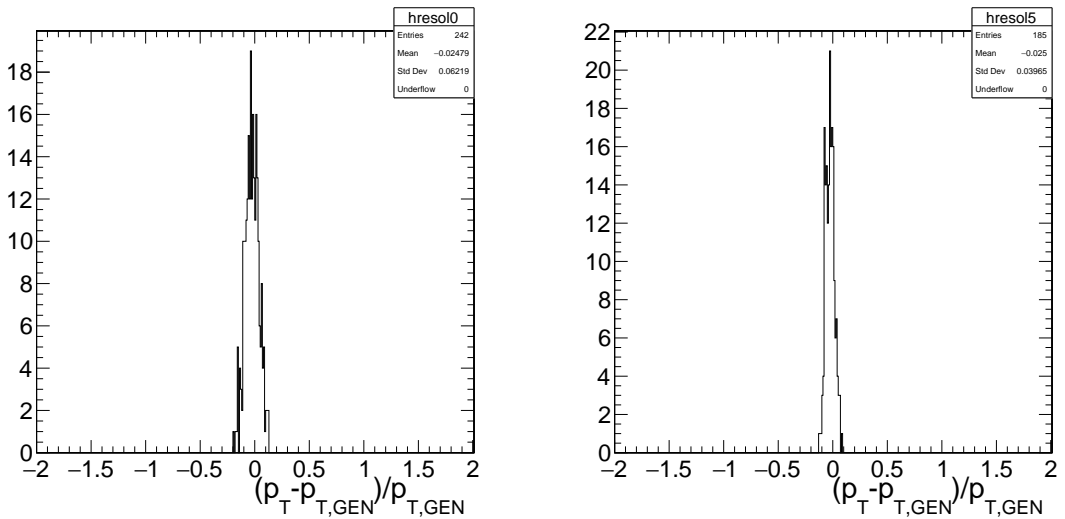


Figure 4.6: The jet energy resolution of neutrons with $0 < |\eta| < 0.5$ and $200 \text{ GeV} < p_T < 300 \text{ GeV}$ (left) or $700 \text{ GeV} < p_T < 800 \text{ GeV}$ (right).

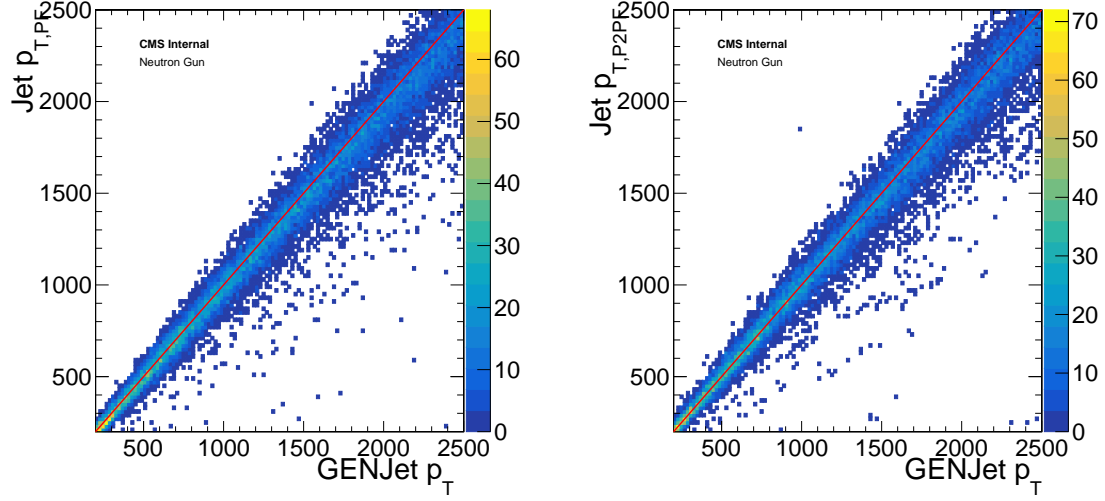


Figure 4.7: Comparison of the transverse momentum of the generator-level jets to the PF jets (left) and P2PF jets (right) in the region $0 < |\eta| < 0.5$ with jet energy resolution smearing, using a neutron sample.

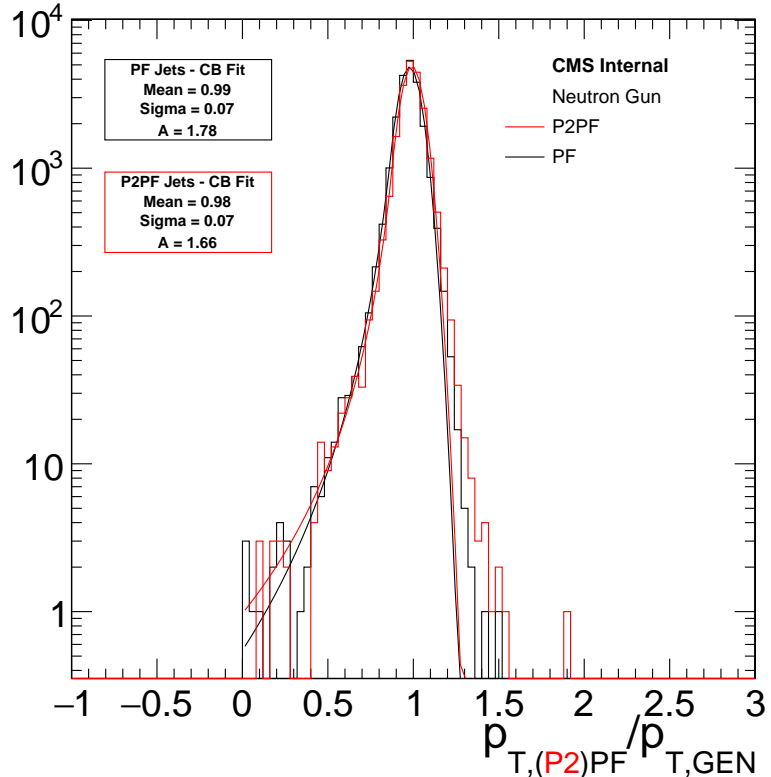


Figure 4.8: The jet energy resolution of the corrected P2PF jets (red) and PF jets (black), fitted with a Crystal Ball function.

5

The Monojet Analysis

¹ **5.1 Introduction**

² **5.2 Event selection**

³ **5.3 Background estimation**

⁴ **5.4 Results**

⁵ **5.5 Improvement going from the 2015 to 2016 analysis**

⁶ **5.6 Interpretation**

6

1

2

Search for SIMPs using Trackless Jets

3 **6.1 Introduction**

4 **6.2 Event selection**

5 **6.3 Background estimation**

6 **6.4 Results**

7 **6.5 SIMP model interpretation**

7

1

2

Conclusion & Outlook

References

- 1
- 2 [1] <http://www.quantumdiaries.org/2014/03/14/the-standard-model-a-beautiful-but-flawed-theory/>
- 3 [2] Q. R. Ahmad et al. *Direct evidence for neutrino flavor transformation from neutral current interactions in the Sudbury Neutrino Observatory*. Phys. Rev. Lett., 89:011301, 2002.
- 4
- 5 [3] Y. Fukuda et al. *Evidence for oscillation of atmospheric neutrinos*. Phys. Rev. Lett., 81:1562–1567, 1998.
- 6
- 7 [4] Gianfranco Bertone, Dan Hooper, and Joseph Silk. *Particle dark matter: Evidence, candidates and constraints*. Phys. Rept., 405:279–390, 2005.
- 8
- 9 [5] F. Zwicky. *Die Rotverschiebung von extragalaktischen Nebeln*. Helv. Phys. Acta, 6:110–127, 1933.
- 10 [Gen. Rel. Grav. 41, 207(2009)].
- 11 [6] K. G. Begeman, A. H. Broeils, and R. H. Sanders. *Extended rotation curves of spiral galaxies: Dark haloes and modified dynamics*. Mon. Not. Roy. Astron. Soc., 249:523, 1991.
- 12
- 13 [7] P. Salucci and A. Borriello. *The intriguing distribution of dark matter in galaxies*. Lect. Notes Phys., 616:66–77, 2003.
- 14
- 15 [8] Arno A. Penzias and Robert Woodrow Wilson. *A Measurement of excess antenna temperature at 4080-Mc/s*. Astrophys. J., 142:419–421, 1965.
- 16
- 17 [9] M. Azzaro, F. Prada, and C. M. Gutierrez. *Motion properties of satellites around external spiral galaxies*. ASP Conf. Ser., 327:268, 2004.
- 18
- 19 [10] Mario Mateo. *Dwarf galaxies of the Local Group*. Ann. Rev. Astron. Astrophys., 36:435–506, 1998.
- 20
- 21 [11] John N. Bahcall, Chris Flynn, and Andrew Gould. *Local dark matter from a carefully selected sample*. Astrophys. J., 389:234–250, 1992.
- 22
- 23 [12] V. M. Lobashev. *The search for the neutrino mass by direct method in the tritium beta-decay and perspectives of study it in the project KATRIN*. Nucl. Phys., A719:153–160, 2003.
- 24
- 25 [13] V. N. Aseev et al. *An upper limit on electron antineutrino mass from Troitsk experiment*. Phys. Rev., D84:112003, 2011.
- 26
- 27 [14] Ch. Kraus et al. *Final results from phase II of the Mainz neutrino mass search in tritium beta decay*. Eur. Phys. J., C40:447–468, 2005.
- 28
- 29 [15] M. C. Gonzalez-Garcia and Yosef Nir. *Neutrino masses and mixing: Evidence and implications*. Rev. Mod. Phys., 75:345–402, 2003.
- 30
- 31 [16] Scott Dodelson and Lawrence M. Widrow. *Sterile-neutrinos as dark matter*. Phys. Rev. Lett., 72:17–20, 1994.
- 32
- 33 [17] David N. Spergel and Paul J. Steinhardt. *Observational evidence for selfinteracting cold dark matter*. Phys. Rev. Lett., 84:3760–3763, 2000.
- 34 [18] James S. Bullock. *Notes on the Missing Satellites Problem*. 2010.

- 1 [19] Michael Boylan-Kolchin, James S. Bullock, and Manoj Kaplinghat. *Too big to fail? The puzzling*
2 *darkness of massive Milky Way subhaloes.* Mon. Not. Roy. Astron. Soc., 415:L40, 2011.
- 3 [20] David H. Weinberg, James S. Bullock, Fabio Governato, Rachel Kuzio de Naray, and Annika H. G.
4 Peter. *Cold dark matter: controversies on small scales.* Proc. Nat. Acad. Sci., 112:12249–12255,
5 2014. [Proc. Nat. Acad. Sci.112,2249(2015)].
- 6 [21] Benoit Famaey and Stacy McGaugh. *Challenges for Lambda-CDM and MOND.* J. Phys. Conf.
7 Ser., 437:012001, 2013.
- 8 [22] J. F. Donoghue, E. Golowich, and Barry R. Holstein. *Dynamics of the standard model.* Camb.
9 Monogr. Part. Phys. Nucl. Phys. Cosmol., 2:1–540, 1992. [Camb. Monogr. Part. Phys. Nucl. Phys.
10 Cosmol.35(2014)].
- 11 [23] C. Downum, T. Barnes, J. R. Stone, and E. S. Swanson. *Nucleon-meson coupling constants and*
12 *form-factors in the quark model.* Phys. Lett., B638:455–460, 2006.
- 13 [24] Scott W. Randall, Maxim Markevitch, Douglas Clowe, Anthony H. Gonzalez, and Marusa Bradac.
14 *Constraints on the Self-Interaction Cross-Section of Dark Matter from Numerical Simulations of the*
15 *Merging Galaxy Cluster 1E 0657-56.* Astrophys. J., 679:1173–1180, 2008.
- 16 [25] Jonathan L. Feng. *Dark Matter Candidates from Particle Physics and Methods of Detection.* Ann.
17 Rev. Astron. Astrophys., 48:495–545, 2010.
- 18 [26] Gregory D. Mack, John F. Beacom, and Gianfranco Bertone. *Towards Closing the Window on*
19 *Strongly Interacting Dark Matter: Far-Reaching Constraints from Earth’s Heat Flow.* Phys. Rev.,
20 D76:043523, 2007.
- 21 [27] J. Rich, R. Rocchia, and M. Spiro. *A Search for Strongly Interacting Dark Matter.* Phys. Lett.,
22 B194:173, 1987. [,221(1987)].
- 23 [28] Adrienne L. Erickcek, Paul J. Steinhardt, Dan McCammon, and Patrick C. McGuire. *Constraints*
24 *on the Interactions between Dark Matter and Baryons from the X-ray Quantum Calorimetry Experi-*
25 *ment.* Phys. Rev., D76:042007, 2007.
- 26 [29] Gregory D. Mack and Adithya Manohar. *Closing the window on high-mass strongly interacting*
27 *dark matter.* J. Phys., G40:115202, 2013.
- 28 [30] Richard H. Cyburt, Brian D. Fields, Vasiliki Pavlidou, and Benjamin D. Wandelt. *Constraining*
29 *strong baryon dark matter interactions with primordial nucleosynthesis and cosmic rays.* Phys.
30 Rev., D65:123503, 2002.
- 31 [31] Xue-lei Chen, Steen Hannestad, and Robert J. Scherrer. *Cosmic microwave background and large*
32 *scale structure limits on the interaction between dark matter and baryons.* Phys. Rev., D65:123515,
33 2002.
- 34 [32] Cora Dvorkin, Kfir Blum, and Marc Kamionkowski. *Constraining Dark Matter-Baryon Scattering*
35 *with Linear Cosmology.* Phys. Rev., D89(2):023519, 2014.
- 36 [33] H. Richard Gustafson, Cyril A. Ayre, Lawrence W. Jones, Michael J. Longo, and P. V. Ra-
37 *mania Murthy.* *Search for New Massive Long-lived Neutral Particles.* Phys. Rev. Lett., 37:474,
38 1976.
- 39 [34] K. A. Olive et al. *Review of Particle Physics.* Chin. Phys., C38:090001, 2014.
- 40 [35] N. Daci, Isabelle De Bruyn, S. Lowette, M. H. G. Tytgat, and B. Zaldivar. *Simplified SIMPs and the*
41 *LHC.* JHEP, 11:108, 2015.
- 42 [36] David Aaron Matzner Dominguez, D. Abbaneo, K. Arndt, N. Bacchetta, A. Ball, E. Bartz, W. Bertl,
43 G. M. Bilei, G. Bolla, H. W. K. Cheung, et al. *CMS Technical Design Report for the Pixel Detector*
44 *Upgrade.* 2012.

- 1 [37] Serguei Chatrchyan et al. *Energy Calibration and Resolution of the CMS Electromagnetic Calorimeter in pp Collisions at $\sqrt{s} = 7$ TeV*. JINST, 8:P09009, 2013. [JINST8,9009(2013)].
- 2
- 3 [38] S. Chatrchyan et al. *The CMS Experiment at the CERN LHC*. JINST, 3:S08004, 2008.
- 4
- 5 [39] A. Tapper and Darin Acosta. *CMS Technical Design Report for the Level-1 Trigger Upgrade*. 2013.
- 6
- 7 [40] Jean-marc Olivier Andre, Ulf Behrens, James Branson, Philipp Maximilian Brummer, Olivier Chaze, Sergio Cittolin, Cristian Contescu, Benjamin Gordon Craigs, Georgiana Lavinia Darlea, Christian Deldicque, Zeynep Demiragli, Marc Dobson, Nicolas Doualot, Samim Erhan, Jonathan Richard Fulcher, Dominique Gigi, Maciej Szymon Gladki, Frank Glege, Guillermo Gomez Ceballos, Jeroen Guido Hegeman, Andre Georg Holzner, Mindaugas Janulis, Raul Jimenez Estupinan, Lorenzo Masetti, Franciscus Meijers, Emilio Meschi, Remigius Mommsen, Srecko Morovic, Vivian O'Dell, Luciano Orsini, Christoph Maria Ernst Paus, Petia Petrova, Marco Pieri, Attila Racz, Thomas Reis, Hannes Sakulin, Christoph Schwick, Dainius Simelevicius, Petr Zejdl, Hamburg, California, San Diego, California, Chicago, Illinois, Massachusetts Institute of Technology, Cambridge, Massachusetts, also at Vilnius University, Vilnius, Lithuania, and also at. *Performance of the CMS Event Builder*. Technical Report CMS-CR-2017-034, CERN, Geneva, Feb 2017.
- 11
- 12
- 13
- 14
- 15
- 16
- 17 [41] J. Pumplin, D. R. Stump, J. Huston, H. L. Lai, Pavel M. Nadolsky, and W. K. Tung. *New generation of parton distributions with uncertainties from global QCD analysis*. JHEP, 07:012, 2002.
- 18
- 19 [42] A. D. Martin, W. J. Stirling, R. S. Thorne, and G. Watt. *Parton distributions for the LHC*. Eur. Phys. J., C63:189–285, 2009.
- 20
- 21 [43] Richard D. Ball et al. *Parton distributions for the LHC Run II*. JHEP, 04:040, 2015.
- 22
- 23 [44] J. Alwall, R. Frederix, S. Frixione, V. Hirschi, F. Maltoni, O. Mattelaer, H. S. Shao, T. Stelzer, P. Torrielli, and M. Zaro. *The automated computation of tree-level and next-to-leading order differential cross sections, and their matching to parton shower simulations*. JHEP, 07:079, 2014.
- 24
- 25 [45] Stefano Frixione, Paolo Nason, and Carlo Oleari. *Matching NLO QCD computations with Parton Shower simulations: the POWHEG method*. JHEP, 11:070, 2007.
- 26
- 27 [46] V. N. Gribov and L. N. Lipatov. *Deep inelastic e p scattering in perturbation theory*. Sov. J. Nucl. Phys., 15:438–450, 1972. [Yad. Fiz.15,781(1972)].
- 28
- 29 [47] Yuri L. Dokshitzer. *Calculation of the Structure Functions for Deep Inelastic Scattering and e+ e- Annihilation by Perturbation Theory in Quantum Chromodynamics*. Sov. Phys. JETP, 46:641–653, 1977. [Zh. Eksp. Teor. Fiz.73,1216(1977)].
- 30
- 31
- 32 [48] Guido Altarelli and G. Parisi. *Asymptotic Freedom in Parton Language*. Nucl. Phys., B126:298–318, 1977.
- 33
- 34 [49] Torbjörn Sjöstrand, Stephen Mrenna, and Peter Skands. *PYTHIA 6.4 physics and manual*. JHEP, 05:026, 2006.
- 35
- 36 [50] John Allison et al. *Geant4 developments and applications*. IEEE Trans. Nucl. Sci., 53:270, 2006.
- 37
- 38 [51] Serguei Chatrchyan et al. *Description and performance of track and primary-vertex reconstruction with the CMS tracker*. JINST, 9(10):P10009, 2014.
- 39
- 40 [52] A. Strandlie and R. Fruhwirth. *Discrimination between different types of material in track reconstruction with a Gaussian-sum filter*. IEEE Trans. Nucl. Sci., 53:3842–3849, 2006.
- 41
- 42 [53] Matteo Cacciari, Gavin P. Salam, and Gregory Soyez. *The anti- k_t jet clustering algorithm*. Journal of High Energy Physics, 2008(04):063, 2008.

- ¹ [54] Adam Alloul, Neil D. Christensen, Céline Degrande, Claude Duhr, and Benjamin Fuks. *FeynRules*
² *2.0 - A complete toolbox for tree-level phenomenology*. Comput.Phys.Commun., 185:2250–2300,
³ 2014.

List of Acronyms

1

2

3

A

4

5
6 ATLAS Almost Toroidal LHC ApparatuS

7

8

B

9

10
11 BU Builder Unit

12

13

C

14

15
16 CERN European Organization for Nuclear Research
17 CHS charged hadron subtraction
18 CMB Cosmic Microwave Background
19 CMS Compact Muon Solenoid
20 CSC Cathode Strip Chambers

21

22

D

23

24
25 DAQ data acquisition
26 DQM Data Quality Monitoring
27 DT Drift Tubes

28

29

E

30

31
32 ECAL electromagnetic calorimeter

33

34

F

35

36
37 FED Front End Driver
38 FSR final state radiation
39 FU Filter Unit

1

2

G

3

5 GSF

Gaussian-sum filter

6

7

H

8

10 HCAL

hadronic calorimeter

11 HLT

High-Level Trigger

12

13

I

14

16 IP

interaction point

17 ISR

initial state radiation

18

19

J

21

22 JER

jet energy resolution

23

24

L

25

26

27 L1

Level-1

28 LEIR

Low Energy Ion Ring

29 LEP

Large Electron Positron

30 LHC

Large Hadron Collider

31 LO

leading order

32

33

N

34

35

36 NLO

next-to-leading order

37

38

P

39

40

41 PDF

parton distribution function

42 PF

particle flow

43 PS

Proton Synchrotron

44 PSB

Proton Synchrotron Booster

1

2

Q

3

4

5 QCD

Quantum Chromodynamics

6

7

R

8

10 RF

radio-frequency

11 ROC

read-out chip

12 RPC

Resistive Plate Chambers

13 RU

Readout Unit

14

15

S

16

18 SIDM

self-interacting dark matter

19 SIMP

strongly interacting massive particle

20 SPS

Super Proton Synchrotron

21 SUSY

supersymmetry

22

23

T

24

26 TEC

Tracker EndCaps

27 TIB

Tracker Inner Barrel

28 TID

Tracker Inner Disks

29 TOB

Tracker Outer Barrel

30

31

W

32

34 WIMP

weakly interacting massive particle

